

Gravitational-wave bursts and stochastic background from superfluid vortex avalanches during pulsar glitches

L. Warszawski^{1*} and A. Melatos¹

¹*School of Physics, University of Melbourne, Parkville, VIC 3010, Australia*

24 May 2021

ABSTRACT

The current-quadrupole gravitational-wave signal emitted during the spin-up phase of a pulsar glitch is calculated from first principles by modeling the vortex dynamics observed in recent Gross-Pitaevskii simulations of pinned, decelerating quantum condensates. Homogeneous and inhomogeneous unpinning geometries, representing creep- and avalanche-like glitches, provide lower and upper bounds on the gravitational wave signal strength respectively. The signal arising from homogeneous glitches is found to scale with the square root of glitch size, whereas the signal from inhomogeneous glitches scales proportional to glitch size. The signal is also computed as a function of vortex travel distance and stellar angular velocity. Convenient amplitude scalings are derived as functions of these parameters. For the typical astrophysical situation, where the glitch duration (in units of the spin period) is large compared to the vortex travel distance (in units of the stellar radius), an individual glitch from an object 1 kpc from Earth generates a wave strain of $10^{-24}[(\Delta\omega/\omega)/10^{-7}](\omega/10^2 \text{ rad s}^{-1})^3(\Delta r/10^{-2} \text{ m})^{-1}$, where Δr is the average distance travelled by a vortex during a glitch, $\Delta\omega/\omega$ is the fractional glitch size, and ω is the pulsar angular velocity. The non-detection of a signal from the 2006 Vela glitch in data from the fifth science run conducted by the Laser Interferometer Gravitational-Wave Observatory implies that the glitch duration exceeds $\sim 10^{-4}$ ms. This represents the first observational lower bound on glitch duration to be obtained.

Key words: dense matter gravitational waves stars: neutron pulsars: general stars: rotation

1 INTRODUCTION

Glitches are stochastic spin-up events that interrupt the smooth electromagnetic spin down of a pulsar. They are commonly attributed to the simultaneous, transitory unpinning and outward motion of between 10^7 and 10^{15} quantised superfluid vortices (Anderson & Itoh 1975; Anderson et al. 1982; Alpar & Sauls 1988; Cheng et al. 1988; Link & Epstein 1996; Warszawski & Melatos 2008; Melatos & Warszawski 2009), which pin metastably to nuclei in the crystalline inner crust (Pines et al. 1980) except during a glitch. The internal superfluid reorganises its velocity field nonaxisymmetrically during such an event, driving a time-varying current quadrupole moment, which emits gravitational radiation.

Pulsar glitches are sources of both burst and continuous gravitational waves. Previous theoretical and observational studies identified the post-glitch recovery phase, dur-

ing which the viscous fluid component comes into corotation with the crust, as a continuous-wave source, with particular attention paid to how the shear viscosity, charged fluid fraction and mutual friction parameter of neutron stars may be extracted from the prospective signal (Andersson & Comer 2001; Peralta et al. 2006a; van Eysden & Melatos 2008; Bennett et al. 2010). A new search algorithm, based on frequency-time maps of cross-power between two spatially separated terrestrial detectors, was proposed recently to identify ‘long transient’ events lasting from seconds to weeks like post-glitch relaxation (Thrane et al. 2010), along with a multi-detector Bayesian algorithm using \mathcal{F} -statistic amplitude priors (Prix et al. 2011).

The burst signal may be split into two categories. The first category includes radiation from inertial r -mode oscillations (Glampedakis & Andersson 2009) or quasi-radial acoustic and inertial modes involving one or two fluid components (Sidery et al. 2010). The strongest signal is achieved when the velocities of the neutron superfluid and the charged fluid oscillate in anti-phase. For a detector with a spec-

* lila@unimelb.edu.au (LW)

tral noise density of $10^{-24} \text{ Hz}^{-1/2}$ at 103 Hz, the maximum signal-to-noise ratio for a glitch from a pulsar at the distance of Vela is 0.9 (Andersson & Comer 2001). The second category of signal, resulting from sudden superfluid deceleration when many vortices unpin simultaneously and move radially outwards, is discussed in this paper.

Many other theories have been proposed for how this happens. Most glitch mechanisms appeal to the storage of angular momentum in the superfluid interior, followed by its rapid release to the crust in discrete events via the sudden unpinning of superfluid vortices (Anderson & Itoh 1975; Alpar et al. 1984; Haskell et al. 2011). Many ideas have been proposed for how this happens, the main point of distinction being the unpinning trigger. Andersson et al. (2004) suggested that an instability between the viscous and inviscid fluid components, governed by the two fluids' relative velocity, can trigger a glitch. Link & Epstein (1996) invoked a sudden change in the coupling of the two fluid components, following the injection of heat into the interior, for example after a sudden rupture in the star's crust, known as a star quake. Star quakes, in which the crust fails and abruptly lowers its moment of inertia, are also invoked as a stand-alone glitch theory for some objects (Ruderman 1969; Middleditch et al. 2006), although star quakes on their own cannot account for the regular, large glitches observed in pulsars like Vela (Crawford & Demiański 2003).

Gravitational waves result from non-axisymmetric rearrangements of mass and/or momentum field, so different glitch theories predict gravitational wave signals of different form and strength. Therefore it is not possible to predict the form of the glitch gravitational wave signal independently of a glitch model, even though one can place limits on its maximum strength from energy arguments (Andersson & Comer 2001). In this paper, we consider specifically the self-organised, catastrophic unpinning model. The model is inspired by the statistics of glitches [scale-free (power-law) sizes and independent (Poissonian) waiting times], which point to an underlying process involving the collective behaviour of many individual elements (Melatos et al. 2008).

A Bayesian search technique (Clark et al. 2007) was recently applied to data collected during the fifth science run of the Laser Interferometer Gravitational-wave Observatory (LIGO¹) to look for gravitational radiation from quasi-normal mode oscillations excited by a glitch in the Vela pulsar. No signal was detected. The glitch, detected electromagnetically on 12 August, 2006, at the Hartebeesthoek Radio Observatory in South Africa, occurred during a period of five and a half hours during which the two LIGO detectors at Hanford returned high-quality, contiguous data. Data from the third detector at Livingston were not included in the search due to seismic noise. The search returned an upper bound on the intrinsic strain amplitude of between 6.3×10^{-21} and 1.4×10^{-20} , depending on the wave number of the mode (Abadie et al. 2011). Hayama et al. (2008) employed a Monte-Carlo method to study the detection efficiency of possible gravitational waves triggered by the 2006 Vela pulsar glitch. Glitches in Vela recur quasi-periodically, at intervals of approximately three years, so

there is a case for altering the observation schedule to ensure that a world-wide detector network is operational for the next glitch [the most recent Vela glitch occurred in August, 2006 Flanagan & Buchner (2006)].

Radio telescope timing experiments on pulsar glitches reveal power-law-distributed sizes and exponential waiting times. These statistics point to an underlying collective process that transitions between metastable states via vortex unpinning avalanches (Melatos et al. 2008). Quantum mechanical simulations confirm local and global knock-on mechanisms for triggering and sustaining unpinning avalanches (Warszawski et al. 2012). In many models, the avalanches are spatially localised, so the glitch process is intrinsically nonaxisymmetric.

In this paper, we calculate the gravitational wave signal from vortex avalanches during the spin-up phase of a pulsar glitch. Section sec:GPE summarises the first-principles evidence from quantum mechanical simulations, that a broadband gravitational wave signal arises from non-axisymmetric superfluid vortex rearrangement. The simulations consist of numerical solutions of the non-linear Schrödinger equation, known as the Gross-Pitaevskii equation, which describes the dynamics of a Bose-Einstein condensate. Such simulations are limited to small systems containing $\sim 10^2$ vortices. In Sec. 3 onwards we incorporate the generic behaviour observed in the Gross-Pitaevskii simulations into an approximate analytic theory of vortex motion, which is valid for realistically large numbers of vortices. Sections 3 and 4 evaluate the current quadrupole moment generated by spasmodic vortex motion in an idealised neutron star geometry. In Sec. 5, we calculate the gravitational wave signal from the motion of a single vortex. The signal arising from a vortex avalanche is calculated in Sec. 6, including consideration of the avalanche opening angle (Sec. 6.1), vortex speed (Sec. 6.4) and glitch size (6.5). Criteria are given for detecting a gravitational wave burst from an individual glitch. In Sec. 7, we summarise our results and discuss critically the underlying assumptions of the calculation. For completeness, we also explain in the appendix how the theoretical machinery in Sec. 3–6 can be applied to calculate rigorously the glitch contribution to the stochastic gravitational-wave background. The signal-to-noise ratio is small for current- and next-generation detectors, if only Galactic pulsars are considered, but it may be significant when extragalactic objects are included, an interesting avenue for future work.

2 MOTIVATION: QUANTUM MECHANICAL SIMULATIONS

Let us begin by confirming that, at the microscopic level, a quantum condensate (such as the neutron superfluid in the pulsar interior) in a decelerating container undergoes spasmodic vortex reorganisation, which emits a bursty broadband gravitational wave signal. Such systems are traditionally studied by solving the Gross-Pitaevskii equation (GPE), a non-linear Schrödinger equation of the form

$$i\hbar \frac{\partial \psi}{\partial t} = -\frac{\hbar^2}{2m} \nabla^2 \psi + V\psi + |\psi|^2 \psi, \quad (1)$$

where ψ is the two-dimensional order parameter of a zero-temperature Bose-Einstein condensate, from which the con-

¹ <http://www.ligo.org>

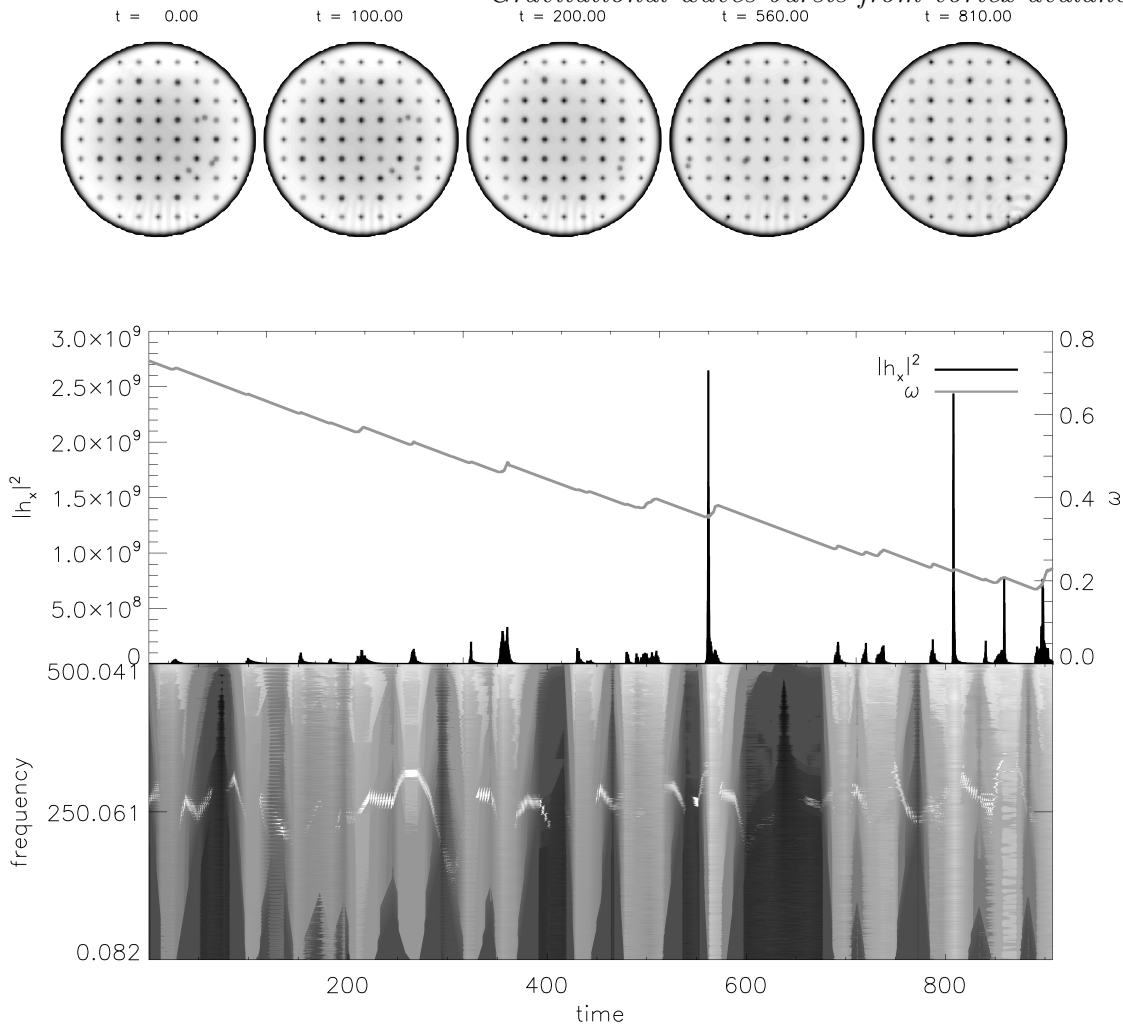


Figure 1. *Top:* Greyscale snapshots of superfluid density $|\psi|^2$ (where ψ is the two-dimensional complex order parameter) at $t = 0, 100, 200, 560$ and 810 (in arbitrary units) from *left to right* respectively. The *darker dots*, and the *lighter dots* that are not part of the rectangular array, are vortices; *lighter dots* in the array are unoccupied pinning sites. *Middle:* Squared modulus of the gravitational wave strain in the cross polarisation $|h_{\times}|^2$ as a function of time t (*black curve* plotted against *left vertical axis*) and angular velocity $\omega(t)$ of the crust as a function of time (*grey curve* plotted against *right vertical axis*) for the simulations described in Sec. 2 (further detail is given in Warszawski & Melatos 2011). *Bottom:* Frequency-time spectrogram of $|h_{\times}|^2$ calculated in time windows of width 12.3. Simulation parameters: $N_c/I_c = 10^{-3.0}$, $V_0 = 16.6$, $\eta = 1$, $\Delta V_i/V_0 = 0.0$, $R = 12.5$, $\Delta x = 0.15$, $\Delta t = 0.0025$, $\omega_0 = 0.8$ (definitions of these quantities appear in Warszawski & Melatos 2011).

densate density, $|\psi|^2$, is derived, and $|\psi|^2\psi$ is the quantum pressure term which governs the structure of vortex cores. V is the potential, which comprises the container that confines the condensate, as well as a grid of spikes, which act as pinning sites for vortices, since the overlap of the empty vortex core with the region emptied of condensate by the high potential results in a low-energy configuration (Avogadro et al. 2008). V also contains a term proportional to the chemical potential. Initially, when the container is accelerated, vortices form and pin to the pinning sites. The initial pinning positions depend on the number of vortices and the number and strength of pinning sites (Sato et al. 2007; Mink et al. 2009; Goldbaum & Mueller 2009; Warszawski & Melatos 2011) and exhibit hysteresis (Jackson & Barenghi 2006).

Previous numerical studies of a vortex lattice, pinned to a decelerating container reveal that vortices hop spasmodically between pinning sites as they move towards the container edge (Warszawski & Melatos 2011). Computational expense limits the system size to tens of vortices, so the results do not translate directly to a realistic pulsar. Instead, we use the qualitative behaviour observed as a basis for analytic extrapolation in later sections, when calculating the gravitational radiation from real glitches.

Our simulations solve the Gross-Pitaevskii equation (GPE) for a zero-temperature condensate in a rotating container. For simplicity, we model an infinite vertical column of superfluid (strictly, its two-dimensional cross-section) in the presence of a rectangular grid of pinning sites. A summary of the technical details is given in Warszawski et al. (2012).

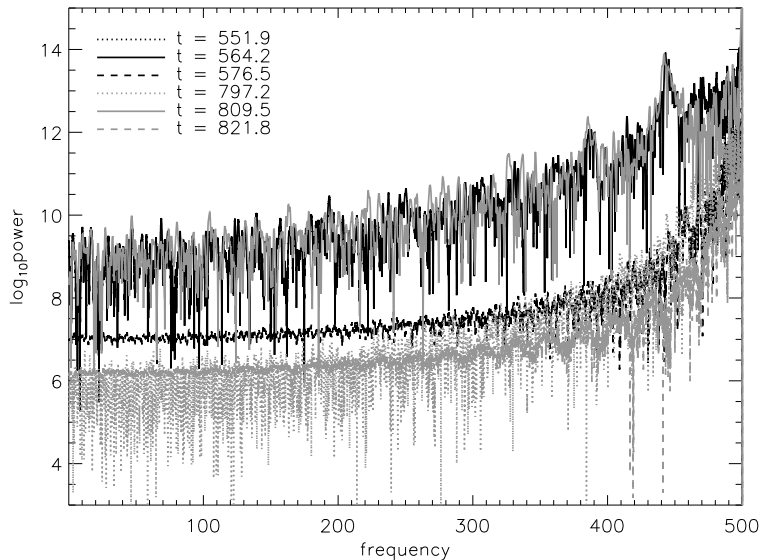


Figure 2. Constant- t cross-sections of the spectrogram of $|h_{\times}|^2$ graphed in Fig. 1, at $t = 551.9, 564.2, 576.5, 797.2, 809.5$ and 821.8 (black dotted, black solid, black dashed, grey dotted, grey solid and grey dashed curves respectively), showing spectral power as a function of frequency on log-linear axes (arbitrary units).

The initial state of the system, depicted in the *top left* image of Fig. 1 (a greyscale snapshot of superfluid density), comprises 12 pinned vortices (*darker dots*) and 38 unoccupied pinning sites (*lighter dots*). An external spin-down torque is then applied to the container, imitating the electromagnetic spin-down torque acting on a pulsar. Pinning prevents vortices from moving radially outwards, fostering an angular velocity mismatch between the superfluid and container. In response, vortices hop between pinning sites in spasmodic bursts, releasing discrete parcels of angular momentum to the container. The images in the *top* panel of Fig. 1 depict the superfluid density at $t = 0, 100, 200, 560$ and 810 (the external torque is turned on at $t = 0$; time is quoted in arbitrary simulation units). We can see that vortices move from their initial positions. For example, the interstitial vortex in the *bottom right* quadrant at $t = 0$ annihilates against the container wall by $t = 560$.

From movies of the time evolution of the superfluid density, we see that the typical vortex trajectory is not simple. As the vortex prepares to unpin, it migrates slowly to the outer edge of its pinning site. It then accelerates off the pinning site, before spiralling into the new pinning site if and when it repins. In later sections, we approximate the radial speed as a parabolic function of time to facilitate analytic calculations. The motion of individual vortices is described in detail in Warszawski et al. (2012).

Each time a vortex moves, the superfluid velocity field adjusts in response. Each vortex generates a solenoidal velocity field, whose magnitude is inversely proportional to distance from the vortex core. The total velocity, \mathbf{v}_s , at any point is the vector sum of the contributions from each vortex. Time-varying nonaxisymmetries in \mathbf{v}_s generate a time-varying current quadrupole moment, resulting in gravitational waves (Thorne 1980; Melatos & Peralta 2010).

We graph the amplitude squared of the wave strain in the cross polarisation, $|h_{\times}|^2$ (in arbitrary units), whose mathematical definition is formalised in Sec. 3, as a *black* curve in the *middle* panel of Fig. 1. The *grey* curve in the same plot tracks the angular velocity of the container, ω . Note that all calculations are performed in the reference frame that co-rotates with the container and pinning grid. Episodes of non-zero $|h_{\times}|^2$ are clearly accompanied by crustal spin-up events, *i.e.* glitches, when ω increases abruptly. Notably, the maximum $|h_{\times}|^2$ during a glitch is not a monotonic function of glitch size (measured as $\Delta\omega/\omega$, the fractional, impulsive change in ω during a glitch). This is an important reminder that the superfluid non-axisymmetry and hence the gravitational wave strain depend on both the number of vortices that move and the degree of asymmetry in their positions within the star. We discuss this further in the context of real pulsar glitches in Sec. 6.

The *bottom* panel of Fig. 1 is a spectrogram of $|h_{\times}|^2$, calculated by finding the power spectrum of $|h_{\times}|^2$ in time windows of width $\Delta t = 12.3$. Since $|h_{\times}|^2$ is calculated in the co-rotating frame, a peak at ω is absent from the homodyned power spectrum. Once again, bright features in the spectrogram (e.g. at $t \approx 560$) coincide with rotational glitches. The peak signal associated with each glitch occurs at the minimum preceding the glitch-induced spin up, for example, where the spikes in $|h_{\times}|^2$ intersect the $\omega(t)$ curve in the *middle* panel. In Fig. 2, we graph instantaneous power spectra from instants before, during, and after the glitches at $t \approx 564$ and $t \approx 809$ (*black* and *grey* curves respectively). All six curves exhibit a broadband burst signal, which increases with frequency, while the overall amplitude scales with $|h_{\times}|^2$. The two *solid* curves exhibit peaks at frequency values 390 and 440, which are absent from the pre-glitch (*dotted*) and post-glitch (*dashed*) curves, suggesting that the peaks are associated with glitch-induced radiation.

The results presented in this section confirm that the motion of vortices through a grid of pinning sites results in a bursty gravitational wave signal. However, we emphasise that a systematic study remains to be done of how the system size and range of pinning site strengths, amongst many other properties, change the gravitational wave signal. Recent results show that once the ratio of pinning sites to vortices exceeds unity, the statistics of spin-up events do not change (Warszawski & Melatos 2011). However, when vortices outnumber pinning sites, pinning no longer dominates the spin-down dynamics of the condensate, resulting in fewer and smaller glitches. An important unanswered physics question is, does a system containing $\sim 10^{19}$ vortices exhibit unpinning avalanches like systems with $\sim 10^2$ vortices? Semi-analytic studies (Melatos & Warszawski 2009) suggest that avalanche dynamics are still possible in large systems, especially when unpinning vortices can trigger further unpinning in a domino-like effect (Warszawski et al. 2012).

3 CURRENT QUADRUPOLE MOMENT

Drawing inspiration from the vortex dynamics observed in recent studies (Warszawski et al. 2012) and the burst gravitational wave signal computed in Fig. 1, we now develop an analytic formalism that facilitates calculation of a gravitational wave signal from glitches involving realistic numbers ($\gtrsim 10^7$) of vortices. We follow the methodology introduced by Thorne (1980) and employed recently in studies of f-mode and turbulence-driven emission (Wasserman 2008; Melatos & Peralta 2010; Bennett et al. 2010; Sidery et al. 2010).

The far-field metric perturbation (wave strain) generated by a superposition of current multipole moments S^{lm} can be written as

$$h_{jk}^{TT} = \frac{G}{Dc^5} \sum_{l=2}^{\infty} \sum_{m=-l}^l T_{jk}^{B2,lm} \frac{\partial^l S^{lm}}{\partial t^l}, \quad (2)$$

in the transverse, traceless gauge, where t is the retarded time, D is the distance from source to observer, and $T_{jk}^{B2,lm}$ is the beam pattern, which is a function of the observer's orientation relative to the source. The physics of the source is housed in S^{lm} . In general, h_{jk}^{TT} also includes contributions from mass multipoles I^{lm} , which may dominate, but they are neglected in this paper, where we model the matter distribution inside a pulsar as incompressible and axisymmetric.

The (l, m) -th multipole moment, $S^{lm}(t)$ (units: kg ms^{-1}), is given by (Thorne 1980; Melatos & Peralta 2010)

$$S^{lm} = c_l \int d^3x Y_{lm}^* r^l \mathbf{x} \cdot \nabla \times (\rho \mathbf{v}_s), \quad (3)$$

where the integral is taken over the entire volume of the source, \mathbf{v}_s and ρ are the fluid velocity and density respectively, Y_{lm}^* is the complex conjugate of the scalar spherical harmonic

$$Y_{lm} = \sqrt{\frac{(2l+1)(l-m)!}{4\pi(l+m)!}} e^{im\phi} P_l^m(\cos\theta), \quad (4)$$

$P_l^m(\cos\theta)$ is the associated Legendre function, and one has

$$c_l = -\frac{32\pi}{(2l+1)!!} \sqrt{\frac{l+2}{2l(l-1)(l+1)}}. \quad (5)$$

In our application, the leading term in the multipole expansion is $l = 2$, for which only the $m = \pm 1$ terms are nonzero [$P_2^1(x) = -3x(1-x^2)^{1/2}$]. We make the simplifying assumption that the flow is purely azimuthal², such that the mass current term $\mathbf{x} \cdot \nabla \times (\rho \mathbf{v}_s)$ in Eq. (3) reduces to $z [\nabla \times (\rho \mathbf{v}_s)]_z$. It is convenient to switch to cylindrical coordinates (R', ϕ', z') , such that, for a sphere of radius R_s , we have

$$S^{21} = \sqrt{\frac{128\pi}{45}} \int_0^{2\pi} d\phi' e^{i\phi'} \times \int_0^{R_s} dR' R' (R_s^2 - R'^2)^{3/2} [\nabla \times \rho \mathbf{v}_s(R')]_z. \quad (6)$$

In Sec. 4 onwards, vortices are treated as discrete carriers of quantised circulation. It is then straight-forward to evaluate $\rho \mathbf{v}_s$ and hence Eq. (6) as a sum over vortices.

Denoting the inclination angle between the rotation axis of the star and the observer's line of sight by ι , and the azimuth of the line of sight by ζ (relative to some reference plane), the polarised components of the wave strain are

$$\begin{aligned} h_+ &= -\frac{G}{2c^5 D (\cos^2 \iota + \cos^2 \zeta \sin^2 \iota)^2} \sqrt{\frac{5}{2\pi}} \\ &\times [(\cos^2 \iota \sin^2 \iota \sin^2 \zeta + \sin^4 \iota (\cos^4 \zeta + \cos^2 \zeta \sin^2 \zeta \\ &\quad + \cos^2 \zeta \cot^2 \iota) \cos^4 \iota (1 + \cos^2 \zeta \tan^2 \iota))] \\ &\times \text{Re} \left\{ \frac{\partial^2 S^{21}}{\partial t^2} \sin \iota \left[i e^{i\zeta} \cos^2 \zeta \sin^2 \iota + i e^{-i\zeta} \cos^2 \iota \right] \right\} \\ h_{\times} &= -\frac{G \sqrt{\cos^2 \iota + \cos^2 \zeta \sin^2 \iota}}{16c^5 D (\cos^2 \iota + \cos^2 \zeta \sin^2 \iota)^2} \sqrt{\frac{5}{2\pi}} \\ &\times \sec \iota [\cos^2 \iota \sin^2 \iota \sin^2 \zeta + \sin^4 \iota \cos^2 \zeta (1 + \cot^2 \iota) \\ &\quad + \cos^4 \iota (1 + \cos^2 \zeta \tan^2 \iota)]^{1/2} \\ &\times \text{Re} \left\{ \frac{\partial^2 S^{21}}{\partial t^2} e^{i\zeta} \sin \iota (5 + 3 \cos 2\iota - 2e^{4i\zeta} \sin^2 \iota) \right\} \end{aligned} \quad (7, 8)$$

The angles ι and ζ enter through T_{jk}^{B2} . For definiteness, we choose $\iota = \pi/3$ and $\zeta = 0$ in most of the figures and applications to follow. In Sec. 4–6, wave-strain estimates are presented mostly for h_{\times} , as one has $h_+ \sim h_{\times}$, except for certain special (and unlikely) observer orientations. In App. A, when calculating the stochastic background, we average over $\iota \in [0, \pi]$ and set $\zeta = 0$ without loss of generality.

4 DISCRETE VORTEX MOTION

A glitch occurs when many vortices simultaneously unpin and move outward in response to a trigger. In this paper, we remain agnostic about the nature of the trigger, a notorious unsolved problem (Anderson & Itoh 1975; Cheng et al. 1988; Jahan-Miri 2005; Melatos & Warszawski 2009; Warszawski et al. 2012).

² Peralta et al. (2006b) showed that this is inaccurate at high Reynolds numbers, when meridional circulation and Kolmogorov-like turbulence set in (Peralta & Melatos 2009; Melatos & Peralta 2010).

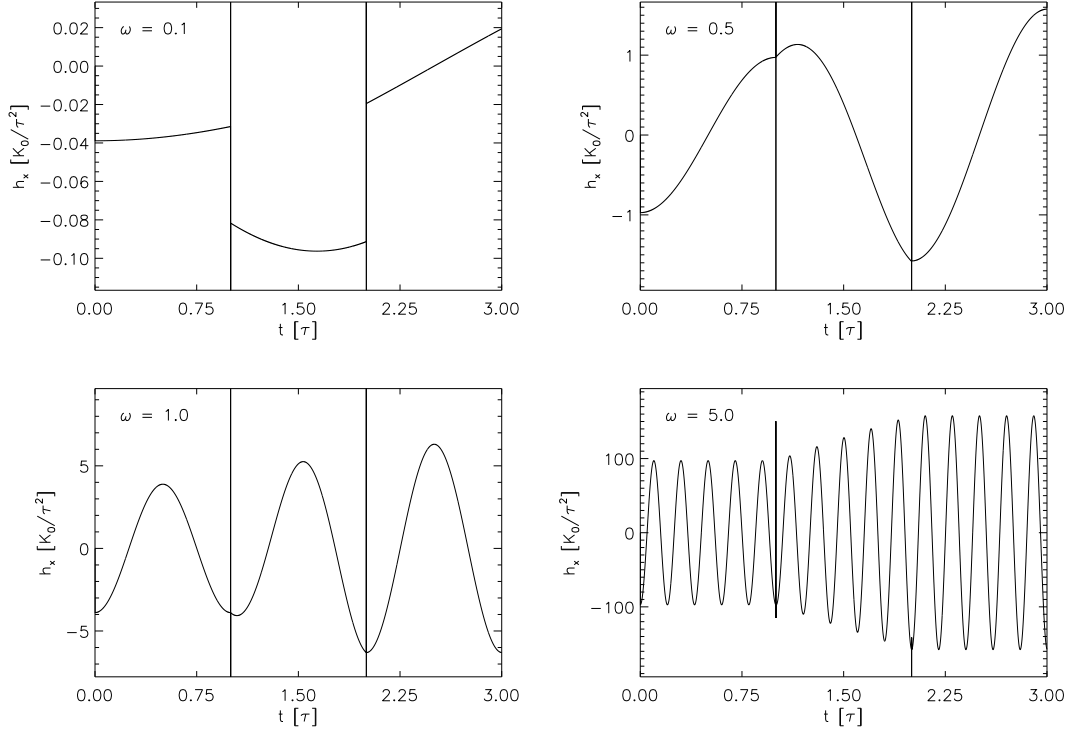


Figure 3. Gravitational wave strain as a function of time in the cross polarisation $h_{\times}(t)$ in units of K_0/τ^2 for a single vortex with initial position $\tilde{R}_0 = 0.1$, which moves a distance $\Delta\tilde{r} = 0.2$, for angular velocity $\tilde{\omega}/(2\pi) = 0.1, 0.5, 1.0$ and 5.0 (*top left, top right, bottom left and bottom right* panel respectively). The vortex unpins at $\tilde{t} = 1$ and repins at $\tilde{t} = 2$ [bracketed by the *vertical spikes* in $h_{\times}(t)$].

Consider ΔN_v vortices that unpin from positions originally arranged in an evenly-spaced array [known as an ‘Abrikosov lattice’, which has hexagonal symmetry (Abrikosov 1957)]. A superfluid is irrotational; it only sustains vorticity at vortex singularities where one has

$$\nabla \times \mathbf{v} = \kappa \delta^{(2)}[\mathbf{x}_{\perp} - \mathbf{x}_{\perp v}(t)] \hat{\mathbf{z}}, \quad (9)$$

for a vortex whose axis runs parallel to the rotation axis and intersects the equatorial plane of the star at $\mathbf{x}_{\perp v}(t)$. Here, $\kappa = h/m = 10^{-7} \text{ m}^2 \text{ s}^{-1}$ is the quantum of circulation, where m is twice the neutron mass. The contribution to S^{21} from a vortex at radius $R_v(t)$ and azimuth $\phi_v(t)$ at time t in a fluid of uniform density ρ is therefore calculated by substituting Eq. (9) into Eq. (6), with the result

$$S^{21} = \frac{1}{3} \sqrt{\frac{512\pi}{45}} \rho \kappa e^{-i\phi_v(t)} R_v(t) [R_s^2 - R_v(t)^2]^{3/2}. \quad (10)$$

Let us define dimensionless variables $\tilde{R}_v = R_v(t)/R_s$, $\tilde{t} = t/\tau$, $\tilde{\phi}_v = \phi_v(t)/(2\pi)$, and $\tilde{\omega} = \omega\tau$, where τ denotes the glitch duration, and R_s is the stellar radius. The radial distance travelled by each vortex between unpinning and repinning is denoted by $\Delta\tilde{r} = \Delta r/R_s$ (dimensionless). It is taken (arbitrarily) to be the same for all vortices and is a parameter of the model, to be evaluated in the future via Gross-Pitaevskii simulations. Hence we write $\tilde{R}_v = \tilde{R}_0 + \tilde{d}(\tilde{t})$ and $\tilde{\phi}_v = \tilde{\phi}_0 + \tilde{\omega}\tilde{t}$, where the initial values are chosen from $\tilde{\phi}_0 \in [0, 1)$ and $\tilde{R}_0 \in [0, 1 - \Delta\tilde{r}]$ respectively. [Unless indicated, symbols used in plot labels are the dimensionless versions (tildes are omitted in plot labels).] In these units

the single-vortex metric perturbation takes the form,

$$h_{jk}^{TT}(R_0, \phi_0, \omega, t) = T_{jk}^{B2,21} \frac{K_0}{\tau^2} e^{-2\pi i \tilde{\phi}_0} \times \frac{\partial^2}{\partial \tilde{t}^2} \left[e^{-2\pi i \tilde{\omega} \tilde{t}} \tilde{R}_v (1 - \tilde{R}_v^2)^{3/2} \right]. \quad (11)$$

Non-glitch pulsar parameters are absorbed in the multiplicative constant

$$K_0 = \frac{G}{c^5 D} \left(\frac{512\pi}{405} \right)^{1/2} \rho \kappa R_s^4, \quad (12)$$

except for $\tilde{\omega}$. The glitch-related parameter τ (vortex travel time) is kept separate.

For a pinned vortex, with $\tilde{d}(\tilde{t}) = 0$ or $\Delta\tilde{r}$, the wave strain reduces to

$$h_{jk}^{TT}(\tilde{R}_0, \tilde{\phi}_0, \tilde{\omega}, \tilde{t}) = -4\pi^2 T_{jk}^{B2,21} \frac{K_0}{\tau^2} e^{-2\pi i(\tilde{\phi}_0 + \tilde{\omega}\tilde{t})} \times \tilde{R}_0 (1 - \tilde{R}_0^2)^{3/2} \tilde{\omega}^2. \quad (13)$$

Equation (13) is therefore the signal emitted by a vortex corotating with the stellar crust. Additionally, in the regime $\tilde{\omega} \gg 1$, where an unpinned vortex moves much further azimuthally than radially during a glitch, Eq. (13) is a good approximation to the wave strain resulting from the outward motion of a single unpinned vortex too.

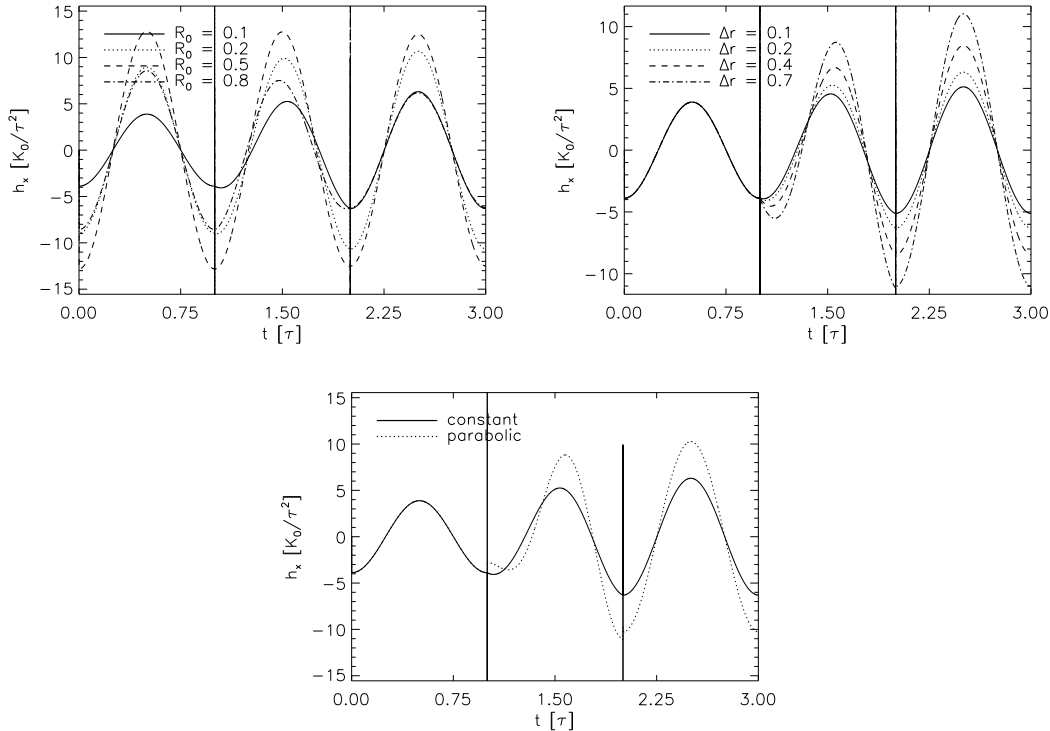


Figure 4. Gravitational wave strain in the cross polarisation as a function of time $h_{\times}(t)$ in units of K_0/τ^2 for a single vortex with $\tilde{\omega}/(2\pi) = 1.0$ as a function of model parameters. *Top left:* Initial radius $\tilde{R}_0 = 0.1, 0.25, 0.5$ and 0.75 , with $\Delta\tilde{r} = 0.2$. *Top right:* Distance moved $\Delta\tilde{r} = 0.1, 0.2, 0.4$ and 0.7 , with $\tilde{R}_0 = 0.1$. *Bottom:* Constant (solid curve) and parabolic (dotted curve) speed profile. All panels have $\tilde{t}_g = 1$.

5 SINGLE VORTEX SIGNAL

In this section, we evaluate $h_{\times}(t)$ for a single vortex as it unpins, moves, and repins. [The results for $h_{+}(t)$ are similar.] We investigate the effect on the wave form of changing ω , R_0 , Δr , and $d(t)$. The radial trajectory is described by

$$\tilde{d}(\tilde{t}) = \begin{cases} 0 & \tilde{t} < \tilde{t}_g \\ \int_{\tilde{t}_g}^{\tilde{t}} d\tilde{t} \tilde{v}_v(\tilde{t}) & \tilde{t}_g \leq \tilde{t} \leq \tilde{t}_g + 1 \\ \Delta\tilde{r} & \tilde{t} > \tilde{t}_g + 1 \end{cases} \quad (14)$$

the vortex starts moving at $\tilde{t} = \tilde{t}_g$. We experiment with both constant and parabolic speed profiles, $\tilde{v}_v(t)$, in what follows. The wave strain is calculated by substituting $\tilde{R}_v = \tilde{R}_0 + \tilde{d}(\tilde{t})$ into Eq. (11).

To begin with, we assume that the speed of the vortex whilst unpinned is constant, i.e. $\tilde{v}_v(\tilde{t}) = \Delta\tilde{r} (\tilde{t}_g \leq \tilde{t} \leq \tilde{t}_g + 1$ and $\tilde{t}_g = 1)$. Figure 3 graphs the wave strain in the cross polarisation $h_{\times}(\tilde{t})$ in units of K_0/τ^2 [see Eq. (12)] for $\tilde{\omega}/(2\pi) = 0.1, 0.5, 1.0$ and 5.0 (*top left, top right, bottom left and bottom right* respectively), corresponding to $0.1, 0.5, 1$ and 5 revolutions during the glitch. In all cases, $\tilde{t}_g = 1$. The graphs extend one time unit beyond when the vortex repins. Even while pinned ($\tilde{t} < 1$ and $\tilde{t} > 2$), a single off-centre vortex produces an oscillatory gravitational wave signal with period $2\pi/\tilde{\omega}$, as its superfluid velocity field is not axisymmetric. Whilst the vortex remains pinned, the zero-to-peak amplitude of the wave strain, h_{\max} , is proportional to $\tilde{\omega}^2$, as described by Eq. (13). While the vortex is moving, h_{\max} changes at a rate $\partial(h_{\max}/K_0)/\partial t =$

$4\pi^2\tilde{\omega}^2(1 - \tilde{R}_v^2)^{3/2} \left[1 - 2\tilde{v}_v/(1 - \tilde{R}_v^2) \right]$. We draw attention to the discontinuous gradient of $h_{\times}(\tilde{t})$ at $\tilde{t} = 1$ and $\tilde{t} = 2$ (even when the vertical jumps are ignored), which occurs because the acceleration is artificially infinite instantaneously. Below we introduce a parabolic speed profile, which smoothes the acceleration and removes the spikes in $h_{\times}(\tilde{t}_g)$ and $h_{\times}(\tilde{t}_g + 1)$.

The shape of the signal does not vary greatly with \tilde{R}_0 . The *top left* panel of Fig. 4 graphs h_{\times} for $0.1 \leq \tilde{R}_0 \leq 0.75$, with fixed $\tilde{\omega}/(2\pi) = 1$ and $\Delta\tilde{r} = 0.2$. The amplitude does not vary monotonically with \tilde{R}_0 , since the term $\rho\mathbf{v}$, which appears in Eq. (6), is a function of the volume-weighted angular velocity (a single vortex does not generate rigid-body rotation). In fact, the amplitude peaks at $\tilde{R}_0 = 0.5$ followed by $\tilde{R}_0 = 0.25, 0.1$ and 0.75 (in descending order). This ordering is preserved whilst the vortex is moving ($1 < \tilde{t} < 2$); however, for $\tilde{t} > 2$, the ordering becomes $\tilde{R}_0 = 0.25, 0.1, 0.5, 0.75$. Notably, the time at which the strain is a maximum for different \tilde{R}_0 is not identical during the glitch. Once again, this feature arises because h_{\times} depends nonlinearly on R_v ; the sinusoidal signal resulting from the rotation of a pinned vortex is amplified or diminished as the vortex moves radially, resulting in a non-sinusoidal signal.

The phase of the signal also varies with $\Delta\tilde{r}$. We graph h_{\times} for different $\Delta\tilde{r}$ in the *top right* panel of Fig. 4, for $\tilde{\omega}/(2\pi) = 1$ and $\tilde{R}_0 = 0.1$ fixed. For each value of $\Delta\tilde{r}$, traversed in unit time, the in-motion wave strain scales proportional to $\Delta\tilde{r}$. Once the vortex repins, the wave strain

Quantity	Value
$\tilde{\omega}/(2\pi)$	1
$\Delta\tilde{\phi}$	0.25
$\Delta\tilde{r}$	0.1
$\Delta\tilde{\omega}/\tilde{\omega}$	0.001
ΔN_v	500

Table 1. Canonical glitch parameters adopted in the simulations in Sec. 6.

amplitude depends on the new radial position $\tilde{R}_0 + \Delta\tilde{r}$, as described by Eq. (13).

Finally, in the *bottom* panel of Fig. 4, we compare the wave strain for a vortex trajectory with a constant (*solid* curve; see above) and parabolic (*dotted* curve) speed profile, viz.

$$\tilde{v}_v(\tilde{t}) = 6\Delta\tilde{r}(\tilde{t} - \tilde{t}_g)[1 - (\tilde{t} - \tilde{t}_g)]. \quad (15)$$

If we ignore the initial spike, a parabolic speed profile results in a higher wave strain, because the maximum \tilde{v}_v is 1.5 times higher than for constant speed.

To summarise, the strongest gravitational wave signal from the motion of a single vortex is achieved when $\tilde{\omega}$ and the maximum vortex speed are high, $\Delta\tilde{r}$ is large, and $\tilde{R}_0 = 0.5$.

6 VORTEX AVALANCHE SIGNAL

6.1 Unpinning geometry

Current glitch detection methods based on radio telescope data are sensitive to glitches involving the simultaneous unpinning and outward motion of at least $\Delta N_v \sim 10^{12}$ vortices. The following approximate formula relates ΔN_v to the fractional frequency jump $\Delta\omega/\omega$ observed:

$$\frac{\Delta\omega}{\omega} \approx \Delta\tilde{r} \frac{\Delta N_v}{N_v} \frac{I_s}{I_c}. \quad (16)$$

It involves the ratio of the superfluid and crust moments of inertia, I_s/I_c (which depends on what fraction of vortices are pinned; $I_s/I_c \sim 10^{-2}$) (Alpar et al. 1989; Epstein & Van Riper 1992), and the total number of vortices $N_v \approx 2\pi\omega R_s^2/\kappa \approx 10^{15} [\omega/(1 \text{ rad s}^{-1})]$.³ Hence $\Delta N_v = 10^{12}$ corresponds to $\Delta\omega/\omega \sim 10^{-11}$, typically the smallest glitch size observed to date (Janssen & Stappers 2006; Melatos et al. 2008; Chukwude & Urama 2010; Espinoza et al. 2011).

The geometry and chronology of a vortex avalanche are vital, yet regrettably unknown, ingredients of the gravitational wave calculation. Do all vortices move simultaneously, from evenly distributed positions throughout the star? Evenly distributed pinning sites with a broad range of pinning potentials represent one possible configuration that would give rise to this scenario (Jones

1991; Melatos & Warszawski 2009). Or, do vortices unpin in a cascade restricted to a wedge within the star (Alpar et al. 1981; Warszawski & Melatos 2008)? A branching process, where an unpinned vortex also preferentially unpins its nearest neighbours, leading to a branching tree of activity, would produce this outcome. We adopt the terms ‘creep-like’ (Alpar et al. 1989) and ‘avalanche-like’ (see Warszawski & Melatos 2008) to describe the former and latter possibilities respectively. During creep-like glitches, the non-axisymmetric change in velocity field due to one vortex largely cancels a similar change from a vortex on the opposite side of the star. Hence we have $\langle h_\times \rangle = 0$ (ensemble average) and the typical strength of the signal in any particular realisation is of order the dispersion $\langle h_\times^2 \rangle^{1/2}$. During avalanche-like glitches, cancellation is incomplete and $\langle h_\times \rangle$ is not zero in general.

In what follows, we calculate only the contribution to the wave strain from vortices that unpin and move during a glitch. In reality, even the static, pinned Abrikosov vortex lattice is not perfectly smooth and axisymmetric: vorticity is carried by point-like vortices rather than in a smooth field. We ignore the small contribution to the wave strain from pinned vortices. In addition, we neglect the contribution from persistent asymmetries in the vortex distribution near the stellar core due to incomplete, stratification-limited Ekman spin up (Bennett et al. 2010).

We perform Monte-Carlo calculations by choosing the initial positions of unpinned vortices at random to investigate the dispersion in h_\times as well as its mean. The *left* panel of Fig. 5 shows the initial vortex configuration for $N_v = 10^4$. Vortices (represented as *dots*) are initially placed in an hexagonal Abrikosov lattice, inside a circle of radius $1 - \Delta\tilde{r}$. The *centre* panel of Fig. 5 shows the vortex positions after a creep-like glitch. The *right* panel shows the positions following an avalanche-like glitch of the same size. The initial positions (\tilde{R}_0 and $\tilde{\phi}_0$) of vortices that unpin are drawn from the following probability distribution functions (PDFs):

$$p(\tilde{R}_0) = 2\tilde{R}_0, \quad (17)$$

$$q(\tilde{\phi}_0) = \frac{1}{\Delta\tilde{\phi}_0} [H(\tilde{\phi}_0 + \Delta\tilde{\phi}_0/2) - H(\tilde{\phi}_0 - \Delta\tilde{\phi}_0/2)], \quad (18)$$

where $H(\cdot)$ is the Heaviside step function, and we choose $\tilde{\phi}_0 = 0$ as the bisector of the avalanche without loss of generality. For creep-like and avalanche-like glitches, we have $\Delta\tilde{\phi}_0 = 1$ and $\Delta\tilde{\phi}_0 < 1$ respectively. We adopt the parabolic speed profile from Eq. (15), so as to avoid discontinuities leading to artificial spikes in the wave strain. A parabolic profile is also a close approximation to the spiral motion of a vortex as it repins, observed in the quantum mechanical simulations described in Sec. 2.

6.2 Wave strain

We now calculate the gravitational wave signal from a vortex avalanche. We evaluate $h_\times(t)$ in two ways: (1) Monte-Carlo simulations, in which ΔN_v , \tilde{R}_0 and $\tilde{\phi}_0$ are drawn from the avalanche size PDF, $g(\Delta\omega/\omega)$, $p(\tilde{R}_0)$ and $q(\tilde{\phi}_0)$ respectively, using Eq. (16) with $I_s/I_c = 1$; and (2) marginalising over the PDFs in Eq. (17) and (18) to obtain the moments of $h_\times(t)$ for fixed $\Delta\omega/\omega$. Since the contribution to h_\times from

³ This approximation assumes that each vortex is responsible for an equal fraction of the total angular momentum of the superfluid, which is not accurate when the vortices are spread evenly from the centre to the edge of the star.

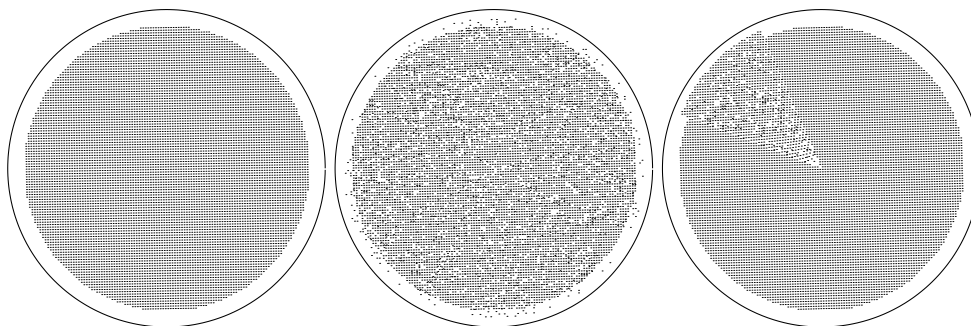


Figure 5. *Left:* Initial vortex positions for 10^4 vortices in an equatorial cross-section of a neutron star. Vortices are confined to radii $\tilde{R} < 1 - \Delta\tilde{r}$ so that unpinned vortices do not leave the star. *Centre:* Final vortex positions after a creep-like glitch. *Right:* Final vortex positions after an avalanche-like glitch with opening angle $\Delta\tilde{\phi} = 1/8$.

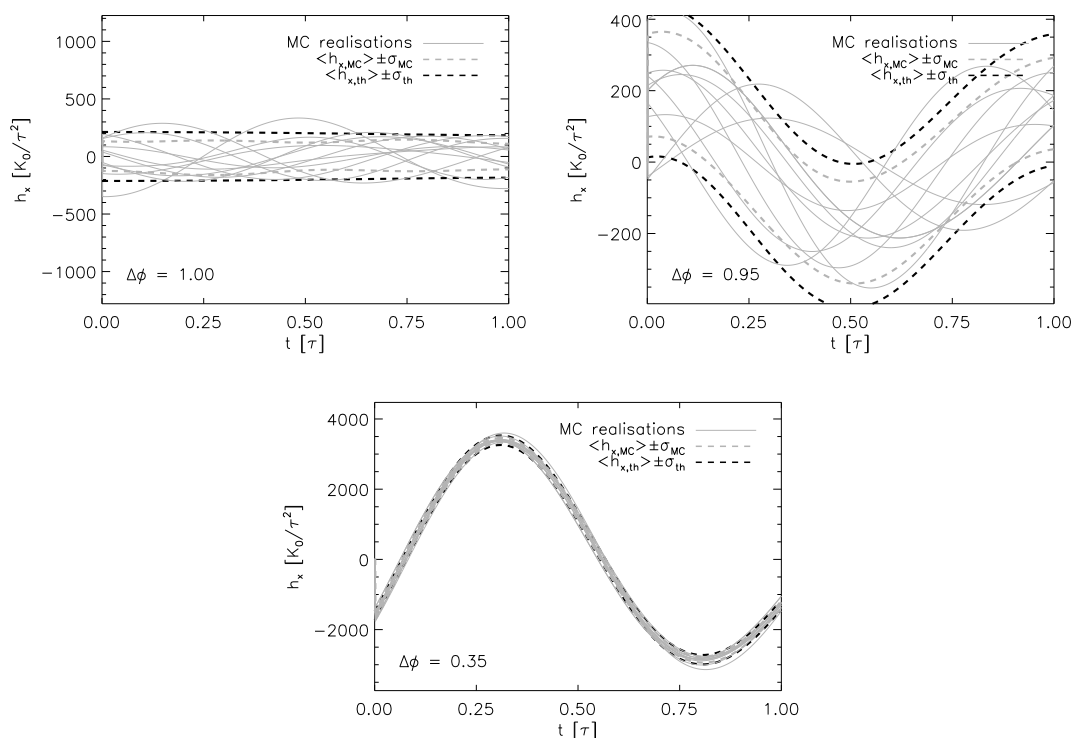


Figure 6. Monte-Carlo results for the wave strain in the cross polarisation as a function of time $h_\times(t)$ for vortex avalanches with opening angles $\Delta\tilde{\phi}_0 = 1.0, 0.95$ and 0.35 (*top left, top right* and *bottom* panels respectively). *Solid grey* curves represent $h_\times(t)$ for 10 different glitch realisations. *Dashed grey* curves display the mean plus/minus one standard deviation of 20 (only 10 are plotted) Monte-Carlo realisations. *Dashed black* curves are theoretical predictions of the mean plus/minus one standard deviation given in Sec. 6.2. Simulation parameters: $N_v = 5 \times 10^4$, $\tilde{\omega}/(2\pi) = 1.0$, $\Delta\tilde{r} = 0.1$.

each vortex is drawn from the same underlying PDF, and these contributions are summed together, the statistics of the aggregate $h_\times(t)$ obey the central limit theorem ($\Delta N_v \gg 1$). That is, at each time t , $h_\times(t)$ is a Gaussian variable with mean $\Delta N_v \mu_1$ and variance $\Delta N_v \sigma_1^2$, where μ_1 and σ_1^2 are the mean and variance respectively of the contribution from a single vortex, given by

$$\mu_1(t) = \frac{2K_0}{\tau^2 \Delta\tilde{\phi}_0} \int_0^{1-\tilde{\Delta}r} d\tilde{R}_0 \tilde{R}_0 \int_{-\Delta\tilde{\phi}/2}^{\Delta\tilde{\phi}/2} d\tilde{\phi}_0 h_{jk}^{TT} \quad (19)$$

$$\sigma_1^2(t) = \langle h_1^2 \rangle - \mu_1^2, \quad (20)$$

$$\langle h_1^2 \rangle(t) = \left(\frac{K_0 \sqrt{2}}{\tau^2 \Delta\tilde{\phi}_0} \right)^2 \int_0^{1-\tilde{\Delta}r} d\tilde{R}_0 \tilde{R}_0 \int_{-\Delta\tilde{\phi}/2}^{\Delta\tilde{\phi}/2} d\tilde{\phi}_0 |h_{jk}^{TT}|^2$$

Here, h_{jk}^{TT} is calculated from Eq. (11). For $\Delta\tilde{\phi}_0 = 1$, Eq. (19) implies $\mu_1 = 0$. However, any particular realisation of the initial vortex positions is not symmetrically distributed around the star, implying $\sigma_1^2 > 0$.

In Fig. 6 we graph $h_\times(t)$ (in units of K_0/τ^2) from 10 glitch realisations (*grey* curves), for $\Delta\tilde{\phi} = 1, 0.95$ and 0.35 (*top left, top right* and *bottom* panels respectively), overplotted with curves representing one standard deviation above

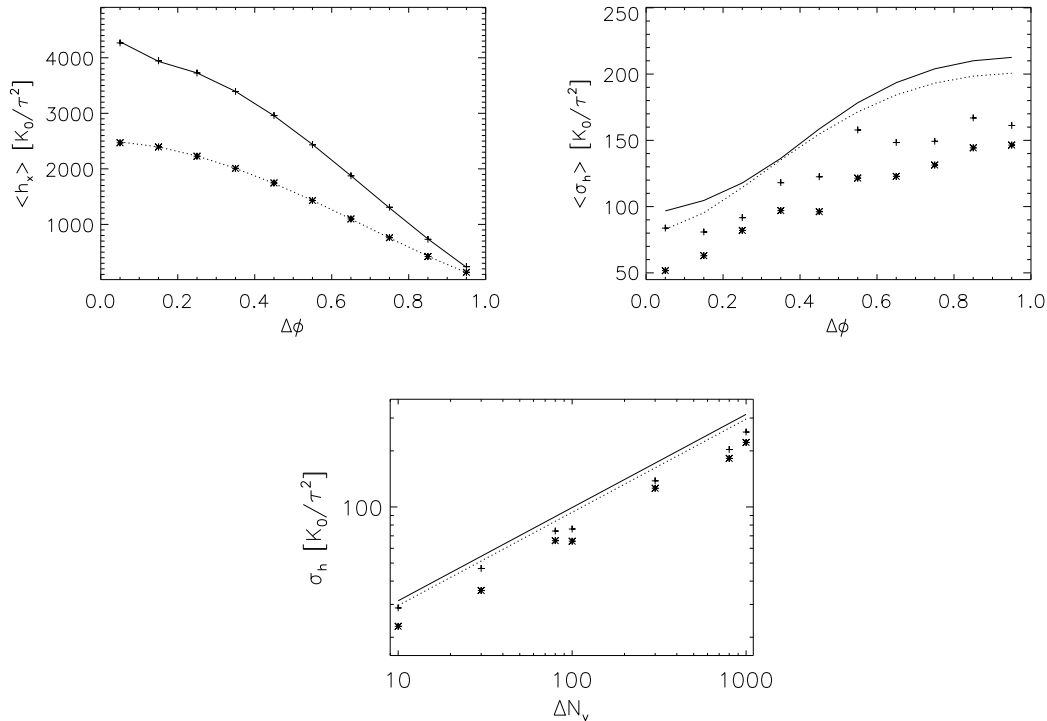


Figure 7. Gravitational wave strain statistics from Monte-Carlo simulations in units of K_0/τ^2 . *Top left:* Maximum (*crosses*) and time-averaged (*asterisks*) $\langle h_x \rangle$ (in units of K_0/τ^2) as a function of avalanche opening angle $\Delta\tilde{\phi}_0$. The *solid* and *dotted* curves are the corresponding analytic predictions. *Top right:* Maximum (*crosses*) and time-averaged (*asterisks*) standard deviation [$\sigma_h = (\langle h_x^2 \rangle - \langle h_x \rangle^2)^{1/2}$] as a function of avalanche opening angle $\Delta\tilde{\phi}_0$. The *solid* and *dotted* curves are the corresponding analytic predictions. *Bottom:* Maximum (*crosses*) and time-averaged (*asterisks*) standard deviation as a function of number of vortices involved in the avalanche, ΔN_v . The *solid* and *dotted* curves are the corresponding analytic predictions.

and below the mean (*dashed grey* curves). Unless otherwise stated, we adopt the set of canonical glitch parameters in Table 1. We compare these curves to the analytic prediction $\Delta N_v \mu_1(t) \pm \sqrt{\Delta N_v} \sigma_1(t)$, given by Eq. (19) and (20) (*dashed black* curves). Both methods of calculation assume that all ΔN_v vortices move simultaneously; in a real avalanche, vortices unpin in a domino chain, but the domino time-scale is rapid compared to the time separation between glitches. Even for 20 realisations, the standard deviation of the Monte-Carlo results, σ_{MC} , deviates from $\sigma_1 \sqrt{\Delta N_v}$ by less than 1% for $\Delta\tilde{\phi} = 0.35$. For $\Delta\tilde{\phi} = 1$, the realisations yield a mean signal that oscillates about zero [Eq. (19) gives precisely zero; our simulations involve a finite number of vortices, resulting in residual dispersion].

The position of the strain maximum, or phase of the signal, varies by up to half a revolution from glitch to glitch. The phase shift appears for the same reason discussed in Sec. 5; the signal amplitude from each vortex in the avalanche is a non-monotonic function of its radial position. For a given ΔN_v , avalanches that are restricted to a thin wedge of the star are more likely than avalanches in larger regions to involve vortices from all radii, effectively smoothing over this effect; for $\Delta\tilde{\phi} \ll 1$, the phase difference between different realisations is negligible.

In order to systematically parametrise the gravitational wave signal, we define four quantities ($\langle \cdot \rangle$ denotes an ensemble

average over realisations and σ_h is the standard deviation of the glitch signal from many vortices).

- (1) The time-averaged mean, $\langle h_x \rangle = \tau^{-1} \int_0^\tau dt \langle h_x \rangle(t)$.
- (2) The maximum amplitude of the mean $\langle h_x \rangle_{\max} = \max\{\langle h_x \rangle(t) | t \in [0, \tau]\}$.
- (3) The time-averaged standard deviation, $\langle \sigma_h \rangle = \tau^{-1} \int_0^\tau \sigma_h(t) dt$.
- (4) The maximum amplitude of the standard deviation, $\sigma_{\max} = \max\{\sigma_h | t \in [0, \tau]\}$.

The *top* panels of Fig. 7 graph these parameters as a function of $\Delta\tilde{\phi}$. For $\langle h_x \rangle$ and $\langle h_x \rangle_{\max}$, Eq. (19) conforms exactly to the Monte-Carlo output (see *left* panel). The signal strength is a decreasing function of the avalanche opening angle: as $\Delta\tilde{\phi}$ increases, it is more likely that the signal from the motion of one vortex interferes destructively with that of another vortex on the other side of the star. The *top right* panel shows that, for $\Delta\tilde{\phi} \gtrsim 0.3$, $\langle h_x \rangle$ decreases linearly with $\Delta\tilde{\phi}$. Both $\langle \sigma_h \rangle$ and σ_{\max} are increasing functions of $\Delta\tilde{\phi}$ for $\Delta\tilde{\phi} \lesssim 0.5$. For $\Delta\tilde{\phi} \gtrsim 0.5$, $\langle \sigma_h \rangle$ and σ_{\max} saturate, since the avalanche spans more than half the star, and hence the motion of vortices on one side of the star start to ‘cancel’ with motion of vortices on the opposite side.

The *bottom* panel of Fig. 7 graphs $\langle \sigma_h \rangle$ and σ_{\max} as functions of ΔN_v . As predicted by the central limit theorem, both quantities increase with the square root of ΔN_v . For glitches involving a significant fraction of the vortices, this

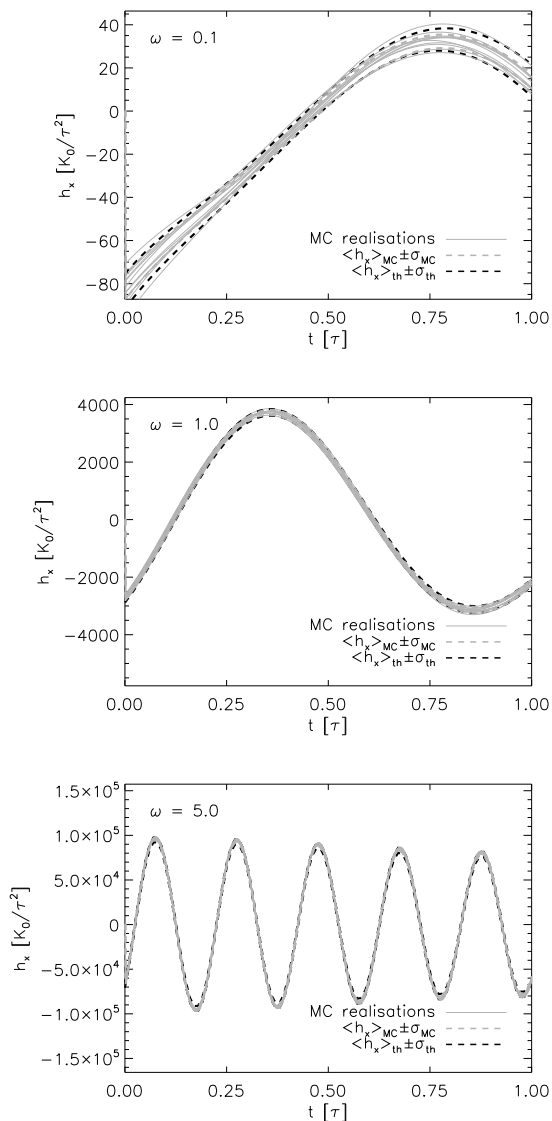


Figure 9. Monte-Carlo results for the wave strain in the cross polarisation as a function of time $h_{\times}(t)$ for angular velocity $\tilde{\omega}/(2\pi) = 0.1, 1.0$ and 5.0 (*top, middle* and *bottom* respectively). *Solid grey* curves represent $h_{\times}(t)$ for different glitch realisations. *Dotted grey* and *dashed grey* curves are the mean and the mean plus/minus one standard deviation of 20 (only 10 are plotted) Monte-Carlo realisations. *Dotted black* and *dashed black* curves are the corresponding analytical predictions. Simulation parameters: $N_v = 5 \times 10^4$, $\Delta\phi_0 = 0.25$, $\Delta\tilde{r} = 0.1$.

trend breaks down, since most of the vortices unpin during the avalanche, not just a small random sample.

In the following sections, we consider avalanches with $\Delta\phi = 0.25$, and explore the change in the mean and standard deviation of the signal as a function of pulsar angular velocity, glitch size, and vortex travel distance.

6.3 Glitch size

Both avalanche and creep-like glitches generate wave strains that scale linearly with glitch size (and hence ΔN_v). In the

top panels of Fig. 8, we graph the mean (*left* panel) and standard deviation (*right* panel) of the wave strain as a function of glitch size, expressed in terms of ΔN_v , for avalanche-like glitches with $\Delta\phi = 0.25$. Both measures of the mean (*top left* panel) introduced in Sec. 6.2 are linearly increasing functions of ΔN_v . The Monte-Carlo (*crosses* and *asterisks*) and analytic (*solid* and *dotted* curves) calculations agree with respect to the means. On the other hand, analytic calculations of $\langle\sigma_h\rangle$ are up to double the Monte-Carlo values, and σ_{\max} does not agree well with Eq. (20), although all calculations respect the scaling $\sigma_{\max} \propto \sqrt{\Delta N_v}$. The same scaling is observed for creep-like glitches, as shown in the *bottom panel* of Fig. 7.

6.4 Vortex travel distance

Glitch size is the product of the number of vortices that unpin and the distance they traverse, according to Eq. (16). In other words, for a given glitch size, either many vortices move a short distance, or few vortices move a large distance. In this section we investigate how the strength of the gravitational wave signal changes with the distance travelled by each vortex, $\Delta\tilde{r}$, to cause a glitch of fixed size.

The *centre* panels of Fig. 8 demonstrate that the mean gravitational wave strength is a decreasing function of $\Delta\tilde{r}$. This result can be understood by noting that increasing the radial distance traversed by each vortex does not make the system more or less asymmetric. Therefore, as $\Delta\tilde{r}$ increases, and ΔN_v decreases in inverse proportion to keep $\Delta\omega/\omega$ constant, we expect the mean and standard deviation to also decrease. This is confirmed by the Monte-Carlo and analytic results in Fig. 8. In calculations not graphed here, we also find that this correlation persists for creep-like glitches.

6.5 Pulsar angular velocity

The mean and dispersion of the wave strain increase with $\tilde{\omega}$; $\langle h_{\times}\rangle$, $\langle h_{\times}\rangle_{\max}$, $\langle\sigma_h\rangle$, and σ_{\max} are plotted versus $\tilde{\omega}$ in the *bottom* panels of Fig. 8. The quantities are quadratic functions of $\tilde{\omega}$, as for a single vortex, e.g. Eq. (13) in Sec. 4.

Figure 9 demonstrates that, for glitches in which azimuthal vortex motion is faster than radial motion, the gravitational wave signal oscillates with the same angular velocity as the pulsar and diminishes with time. For $\tilde{\omega}/(2\pi) < 1$, the signal executes only a fraction of a full oscillation. The variation in the signal results from both azimuthal vortex motion and the changing parabolic vortex speed profile. For example, in the *top* panel of Fig. 9, the signal executes approximately half an oscillation, and the vortex circulates one tenth of the way around the star [$\tilde{\omega}/(2\pi) = 0.1$]. The dependence on $\tilde{\omega}$ is most obvious in the *bottom* panel of Fig. 9, which graphs $h_{\times}(\tilde{t})$ for $\tilde{\omega}/(2\pi) = 5.0$ [*solid grey* curves are Monte-Carlo realisations, *dashed* curves are the mean plus/minus one standard deviation for the Monte-Carlo (*grey*) and analytic (*black*) calculations]. Over the lifetime of the glitch, the amplitude of $\langle h_{\times}\rangle(t)$ decreases by 20%.

From Sec. 5 we know that the signal from a single vortex is a function of its radial position. As a glitch progresses, the mean (taken over all vortices) radial position increases from its initial value $\langle\tilde{R}_v\rangle = 2/3$. Figure 4 demonstrates that,

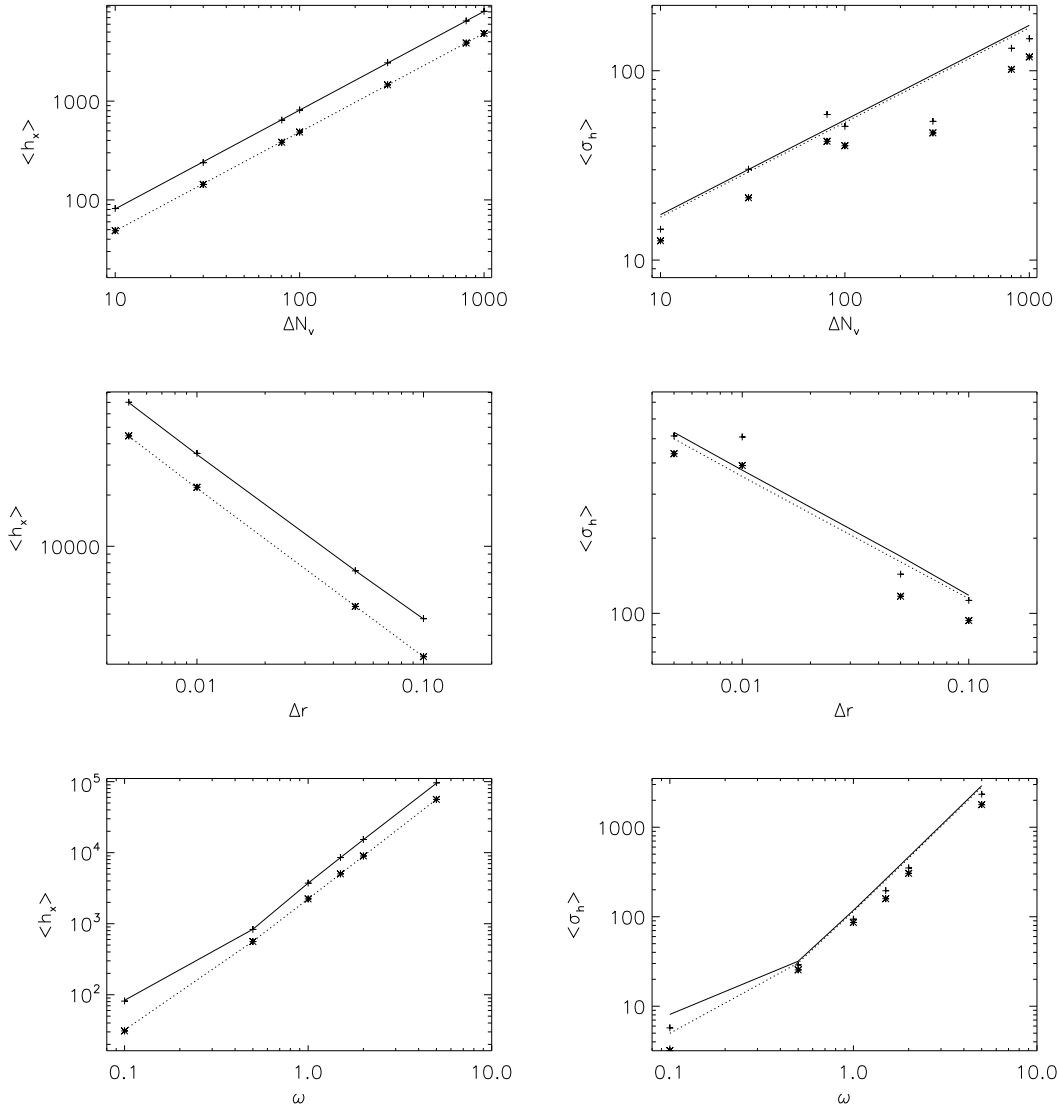


Figure 8. Gravitational wave strain statistics from Monte-Carlo simulations of many-vortex glitches in an individual pulsar. Maximum (*crosses*) and time-averaged (*asterisks*) $\langle h_{\times} \rangle$ (*left*) and $\langle \sigma_h \rangle$ (*right*). The *solid* and *dotted* curves are the corresponding analytic results. The mean and standard deviation are given in units of K_0/τ^2 . *Top*: Variation with the number of vortices that move during the glitch, ΔN_v . *Centre*: Variation with distance travelled by each vortex, $\Delta \tilde{r}$. *Bottom*: Variation with angular velocity, $\tilde{\omega}$.

for $\tilde{R}_v > 0.5$, the maximum signal strength is a decreasing function of \tilde{R}_v , and hence we expect the signal from an avalanche to weaken with time. It is important to note that for a real glitch this effect is expected to be negligible ($\Delta \tilde{r} \ll \langle \tilde{R}_0 \rangle$). As in previous sections, the number of oscillations of $\langle h_{\times} \rangle(t)$ during the avalanche is not precisely $\tilde{\omega}/(2\pi)$, owing to changes in $\langle \tilde{R}_v \rangle$ with time.

6.6 Amplitude scaling

As a guide to how the signal from a single glitch scales with the physical parameters associated with the glitch, we provide a back-of-the-envelope estimate for the maximum wave strain. There are two regimes, determined by the relative size of $\tilde{\omega}$ and $\Delta \tilde{r}$. For $\tilde{\omega} \ll \Delta \tilde{r}$, but keeping $\Delta \tilde{r} \ll 1$ (i.e. the

vortices still travel across only across a very small fraction of the star), the azimuthal motion of the vortices is negligible compared to their radial motion; this scenario arises when the vortex travel time is much shorter than the neutron star rotation period. In this case, the zero-to-peak amplitude of h_{\times} is obtained by setting $d\tilde{R}_v/dt \approx \Delta \tilde{r}/\tau$ and expanding Eq. (11) to first order in $\Delta \tilde{r}$ and is given by

$$\langle h_{\times, \max} \rangle \approx 3 \frac{K_0}{\tau^2} \Delta \tilde{r} \langle \tilde{R}_0 \rangle^2 \Delta N_v \quad (22)$$

$$= 10^{-28} \left(\frac{D}{1 \text{ kpc}} \right)^{-1} \left(\frac{\tau}{10 \text{ ms}} \right)^{-2} \times \left(\frac{\Delta \omega / \omega}{10^{-7}} \right) \left(\frac{\omega}{10^2 \text{ rad s}^{-1}} \right). \quad (23)$$

D and ω are the distance to the source and its angular velocity respectively, and they are pulsar, but not glitch, dependent. τ and Δr are the vortex travel time and distance respectively. We note that both τ and Δr may vary between glitches, and even between individual vortices moving within a single glitch. However, in general, the faster and further vortices move, the stronger the gravitational wave signal. Further studies using first-principles simulations, such as those presented in Sec. 2 and Warszawski et al. (2012), and an understanding of how vortex behaviour scales with system size, are needed to fix these parameters accurately.

Alternatively, for $\tilde{\omega} \gg \Delta\tilde{r}$, but $\tilde{\omega}$ still small, the azimuthal vortex motion is a larger contributor to the wave strain than is the radial motion. The signal amplitude is obtained by expanding Eq. (11) to first order in $\tilde{\omega}$, and scales as

$$\begin{aligned} \langle h_{\times, \max} \rangle &\approx \frac{K_0}{\tau^2} (2\pi\tilde{\omega})^2 \langle \tilde{R}_0 \rangle \Delta N_v & (24) \\ &= 10^{-24} \left(\frac{D}{1 \text{ kpc}} \right)^{-1} \left(\frac{\Delta r}{10^{-2} \text{ m}} \right)^{-1} \\ &\quad \times \left(\frac{\Delta\omega/\omega}{10^{-7}} \right) \left(\frac{\omega}{10^2 \text{ rad s}^{-1}} \right)^3. & (25) \end{aligned}$$

In this regime, corotation of pinned vortices with the crust produces a non-zero signal, provided the superfluid flow is non-axisymmetric, whose strength is a function of the non-uniformity of the vortex configuration (Wasserman 2008), e.g. pinning at grain boundaries (inhomogeneous) versus dislocations and lattice sites (homogeneous). Here, it is important to note that Eq. (25) estimates the strength of the gravitational wave strain from azimuthal vortex motion on the rotation time scale, even though such motion is ongoing, even when the neutron star is not glitching. To avoid the conclusion that there is a strong, persistent signal from rotation of pinned vortices, we must assume that non-axisymmetry in the vortex lattice is much more pronounced when a large number of vortices are not pinned (i.e. during a glitch) than during inter-glitch intervals.

6.7 Example: the 2006 glitch in Vela

We can use Eq. (23) and (25) to constrain the glitch duration for the 2006 Vela glitch. Non-detection of gravitational waves from this glitch (Abadie et al. 2011) put an upper limit of 10^{-20} on the wave strain. For $\tilde{\omega} \ll \Delta\tilde{r}$, with Vela-like parameters ($D \approx 300 \text{ pc}$, $\omega \approx 71 \text{ rad s}^{-1}$, $\Delta\omega/\omega \approx 10^{-6}$ and $\Delta r = 10^{-2} \text{ m}$), the lower bound on the glitch duration is then $\tau \gtrsim 10^{-4} \text{ ms}$. Of course, the independence of τ , Δr and $\Delta\omega/\omega$ cannot be taken for granted. For example, if τ is the time taken for a vortex to travel a distance Δr , which in turn depends on the superfluid-crust velocity lag (through the vortex velocity), then we cannot hold Δr , and even $\Delta\omega/\omega$, constant whilst varying τ . We also remind the reader that underpinning these estimates is the conservative assumption that the pinned vortex distribution is symmetric, apart from those vortices participating in the avalanche. Otherwise there would be a persistent gravitational wave signal described by Eq. (25).

We also note that the $\tilde{\omega} \gg \Delta\tilde{r}$ approximation returns a wave strain that is much stronger than the persistent signal ($h \sim 10^{-31}$) arising from turbulence in a differentially

rotating Crab-like neutron star (Melatos & Peralta 2010). The predicted wave strain resulting from the same physical mechanism operating in a nearby ($D \sim 0.01 \text{ kpc}$), rapidly rotating ($\Omega \sim 3 \times 10^3 \text{ rad s}^{-1}$) neutron star is comparable to our $\tilde{\omega} \gg \Delta\tilde{r}$ scenario [Eq. (25)] for a glitching pulsar (Melatos & Peralta 2010).

7 DISCUSSION

This paper estimates the strength of the gravitational wave burst arising from individual pulsar glitches. Quantum mechanical simulations of rotating, pinned superfluids demonstrate that a broadband burst of gravitational radiation is emitted in the current quadrupole channel by the spasmodic, non-axisymmetric rearrangement of superfluid vortices during a glitch. Generalising the simulation results, which are restricted to systems with $\sim 10^2$ vortices, we employ a discrete model of vortex motion to calculate analytically the wave strain from vortex avalanches involving realistic numbers of vortices ($\sim 10^{12}$).

When a single vortex unpins and moves, the wave strain peaks when the angular velocity and the distance travelled are large, the initial position is half the stellar radius, and the vortex speed is high. Monte-Carlo simulations agree well with analytic calculations. The wave strain depends strongly on the unpinning geometry. If vortices unpin at random throughout the star (vortex creep), the signal is smaller than when unpinning is confined to a thin wedge (vortex avalanche); the maximum wave strain from a glitch of fixed size varies inversely with $\Delta\tilde{\phi}$. In fact, for $\Delta\tilde{\phi} = 1$, the mean wave strain is formally zero.

Quantitatively, the maximum strain is inversely proportional to $\Delta\tilde{r}$, quadratic in $\tilde{\omega}$, and linearly proportional to the number of vortices that unpin and move. The standard deviation of the maximum strain depends on these physical parameters in the same way. We note, however, that for a glitch of a given size, $\Delta\tilde{r}$ and ΔN_v are not independent variables. That is, for fixed $\Delta\tilde{r}$, the number of vortices that unpin and move during a glitch of size s is $\Delta N_v = s N_v I_c / (I_s \Delta\tilde{r})$. We also find that the increase in average radial vortex position as vortices move outward during a glitch damps the amplitude of the glitch gravitational wave signal. This is most apparent for glitches with large ω ; the glitch signal oscillates, and its zero-to-peak amplitude decreases with time. However, in real glitches, the change in average vortex position during a glitch is so small that this effect is negligible.

The wave strain for a glitch in which a vortex travels further azimuthally than radially ($\tilde{\omega} \gg 1$) has a zero-to-peak amplitude $h \sim 10^{-24}$. For a glitch dominated by radial motion ($\tilde{\omega} \ll 1$), the zero-to-peak amplitude is $h \sim 10^{-28}$. These estimates are based on a glitch of size 10^{-7} . Convenient scalings of wave strain with glitch size, stellar angular velocity, vortex travel distance, and glitch duration are presented in Eq. (23) and (25) respectively. We remind the reader that we conservatively assume that vortices that do not move during a glitch do not contribute to the gravitational wave signal. Therefore, when calculating the signal from $\tilde{\omega}$ -dominated vortex motion, we implicitly assume that vortices involved in a glitch are asymmetrically distributed.

Unlike the individual glitch burst signal from a nearby pulsar, which is eminently detectable, the contribution to

the stochastic gravitational wave background is arguably weak. Nevertheless, for completeness, in App. A, we explain how the theoretical machinery in Sec. 3–6 can be applied to calculate the contribution to the background rigorously. Estimates of the strength and spectrum of a stochastic background of gravitational waves resulting from sources of cosmological and astrophysical origin are essential to determining the detectability of burst events and continuous wave sources (Allen & Romano 1999; Ferrari et al. 1999; Regimbau & de Freitas Pacheco 2006b). We find that power-law-distributed glitch sizes (power-law index $-3/2$) from a Galactic population of neutron stars contribute to the stochastic background with a signal-to-noise ratio $\sim 10^{-4}$ (Einstein Telescope). Importantly, however, the inclusion of extra-Galactic pulsars must boost the signal substantially, something that merits careful consideration in a future paper.

The calculations presented here are premised on several assumptions about the physics of glitches and the glitch behaviour of the local neutron star population. Most importantly, our calculation assumes that glitches result from superfluid vortex unpinning avalanches. Alternative glitch theories, such as fluid instabilities (Andersson et al. 2004) and starquakes (Link & Epstein 1996; Negi 2010), generate different signal strengths and spectra. Previous estimates of the maximum achievable signal-to-noise ratio for glitch detections from the energy deposited in f -modes give signal-to-noise ratios $0.4 \lesssim S/N \lesssim 3 \times 10^5$ (Andersson & Comer 2001). The range in S/N is given for a EURO detector including (lower bound) and ignoring (upper bound) shot noise. Larger S/N (up to $\sim 7.4 \times 10^5$) are predicted for instability modes in which the proton and neutron fluids in the stellar core are counter-moving. Abadie et al. (2011) placed Bayesian 90% confidence upper limits on the peak amplitude from the 2006 Vela glitch of 1.4×10^{-20} , corresponding to a maximum energy released through oscillations of the fundamental quadrupole mode of 1.3×10^{35} erg.

Even within the vortex unpinning paradigm, changes to the unpinning physics may alter the estimated gravitational wave signal strength significantly. If, as suggested in the pulsar glitch literature (Melatos et al. 2008; Warszawski et al. 2012), glitches result from a domino effect, then contributions from individual vortices should be summed consecutively and coherently, rather than simultaneously. This is likely to lead to a greater wave strain, as the motion of one vortex is less likely to cancel geometrically with another.

In conclusion, the gravitational wave signal emitted during the spin-up phase of individual glitches resulting from superfluid vortex avalanches is not detectable by current detectors, but it is close as Eq. (25) indicates. Once a detection is made, other informative experiments are possible, e.g. searching for all-sky correlations between the $+$ and \times polarisations. These matters are deferred to future work.

APPENDIX A: STOCHASTIC BACKGROUND

Gravitational waves from neutron star glitches contribute to a stochastic gravitational wave background composed of many unresolved astrophysical sources (Abbott et al. 2009). The Milky Way is populated by $\sim 10^9$ neutron stars, of which $\approx 2 \times 10^3$ have been observed electromagnetically so

far (Manchester et al. 2005). Making some simple assumptions about the glitch rate of the neutron star population as a whole (non-pulsating objects should emit gravitational radiation when they glitch too), we estimate the strength of the glitch background. In this first attempt, we ignore the long-term spin-down evolution of pulsar spins during the lifetime of the Galaxy. We also restrict attention to sources in the Milky Way, as we know nothing about the glitch properties of extra-Galactic neutron stars. With the latter restriction, we find that the Milky Way glitch background is weaker than other LIGO backgrounds. However, the theoretical machinery to calculate the signal, which flows directly from the analysis in Sec. 2-6, is described here for completeness. Simple order-of-magnitude estimates suggest that the background may be significant when extra-Galactic contributions are included, a topic for a future paper.

A1 Total glitch rate

We estimate the total rate of glitches, Θ , by assuming that glitches are manifestations of a self-organised branching process, characterised by a power-law size distribution (Harris 1989; Daly & Porporato 2007)

$$g(s) = (-1/2)(s_+^{-1/2} - s_-^{-1/2})^{-1} s^{-3/2}, \quad (\text{A1})$$

where $s_{\min} \leq s = \Delta\omega/\omega \leq s_+$ is the range of fractional glitch sizes. This distribution is supported qualitatively by observational data for several individual pulsars (Melatos et al. 2008), although it can be shown by a Kolmogorov-Smirnov test on aggregate data that $g(s) \propto s^{-3/2}$ is not universal (Melatos et al. 2008). Across the population, one observes $s_+ \approx 10^{-4}$ and $s_{\min} \approx 10^{-11}$ (the observed minimum glitch size) respectively. The physical lower bound on glitch size, s_- , is given by the fractional change in angular velocity induced by the outward radial motion of a single vortex by a distance characterised by the mean inter-vortex separation $\Delta r \approx [\kappa/(2\omega)]^{1/2}$. Since the total number of vortices in a pulsar is $N_v = 2\pi\omega R_s^2/\kappa$, we obtain

$$s_- = \left(\frac{\kappa}{2\omega}\right)^{1/2} \frac{\kappa}{2\pi\omega R_s^3} \frac{I_s}{I_c} \quad (\text{A2})$$

$$\sim 10^{-23} \left(\frac{\omega}{10^2 \text{ rad s}^{-1}}\right)^{-3/2}. \quad (\text{A3})$$

To proceed, we ask the question, what fraction of glitches are within the observable range? The integrated probability between s_{\min} and s_+ is

$$\int_{s_{\min}}^{s_+} ds g(s) = (s_{\min}^{-1/2} - s_+^{-1/2}) / (s_+^{-1/2} - s_-^{-1/2}) \sim 10^{-7}. \quad (\text{A4})$$

Hence only one in 10^7 glitches is observed by radio telescopes at current sensitivities and for typical observational duty cycles. We now make the simplifying assumption that the glitch rate in each individual pulsar, λ , falls off exponentially with characteristic age [$\lambda(T_c) \propto \exp(-T_c/T_0)$, where T_0 is some reference characteristic age] (Lyne et al. 2000; Melatos et al. 2008), $T_c = \omega/(2\dot{\omega})$, and that neutron stars are being born at a constant rate, leading to a flat distribution of neutron star ages in the galaxy, $p(T_c) = (T_{\max} - T_{\min})^{-1}$. A corollary of this first assumption is that the Crab pulsar ($T_c \approx 10^3$ yr) glitches approximately three times more often than the Vela pulsar ($T_c \approx 10^4$ yr), which

agrees roughly with observations (McKenna & Lyne 1990; Melatos et al. 2008). The PDF of glitch rates is then

$$p(\lambda) = \frac{A}{\lambda^2} (T_{\max} - T_{\min})^{-1}. \quad (\text{A5})$$

Normalisation gives $A \approx 10^3 \text{ yr}^{-2}$, where $T_{\min} = 10^3 \text{ yr}$ and $T_{\max} = 10^{10} \text{ yr}$ are the minimum and maximum age of local neutron stars respectively. The mean glitching rate is then

$$\langle \lambda \rangle = \int_{\lambda_{\min}}^{\lambda_{\max}} d\lambda \lambda p(\lambda) \quad (\text{A6})$$

$$= \frac{A}{T_{\max} - T_{\min}} \ln \left(\frac{T_{\max}}{T_{\min}} \right) \quad (\text{A7})$$

which translates into $\langle \lambda \rangle \sim 10^{-13} \text{ s}^{-1}$ for an individual pulsar. In other words, the mean is dominated by old objects. Given a population of $N_p = 10^9$ pulsars in the Milky Way, the total glitching rate is then

$$\Theta = 10^2 \left(\frac{N_p}{10^9} \right) \left(\frac{\langle \lambda \rangle}{10^{-13} \text{ s}^{-1}} \right) \text{ s}^{-1} \quad (\text{A8})$$

[the factor of 10^7 comes from Eq. (A4), which accounts for unobserved small glitches]. In the next section we see that the relative size of Θ and τ determines the smoothness of the gravitational wave background.

For simplicity, and due to a lack of information, we exclude glitches in extragalactic pulsars from the above discussion. However, we show below that the energy density in gravitational waves is proportional to the aggregate glitch rate in the cosmic volume under consideration, Θ , divided by $\langle D \rangle^2$, the square of the average distance between source and detector. One typically has $\Theta \propto \langle D \rangle^3$ for isotropically distributed sources, suggesting that the contribution from extragalactic pulsars actually dominates. We defer this important calculation to future work. To do it properly, one must account for the redshift-dependent source formation rate and input the statistical properties of extra-galactic neutron stars (Regimbau & de Freitas Pacheco 2006a; Howell et al. 2011; Marassi et al. 2010).

A2 Temporal structure

The character of the stochastic gravitational wave background from pulsar glitches depends on the average number of concurrent glitches, given by $\Theta\tau$. In the regime $\Theta\tau \ll 1$, glitches produce a ‘shot noise’ background of distinguishable burst events. In Sec. 6.6 we place upper and lower bounds on the strength of such distinguishable events. In the opposite regime, $\Theta\tau \gg 1$, glitches generate a continuous (i.e. never absent) background, whose mean and variance we estimate in App. A3. The intermediate regime $\Theta\tau \approx 1$ is often described as ‘popcorn’ noise (Regimbau & de Freitas Pacheco 2006a).

Let us construct the functional form of the background in a time interval of length T , during which ΘT bursts arrive at Earth. The wave strain during this interval is

$$h_{jk}^{TT}(t) = h_1(t - t_1) + h_2(t - t_2) + \dots + h_{\Theta T}(t - t_{\Theta T}), \quad (\text{A9})$$

where t_n is the start time of the n -th glitch, and $h_n(t - t_n)$ is the gravitational wave signal from the n -th glitch. We make the simplifying assumption that the glitch duration, τ , is the same for all glitches, and that the glitch profiles

$h_1(x) = \dots = h_{\Theta T}(x)$ have the same shape but different amplitudes. Continuous and shot noise arise from situations with $\langle t_n - t_{n-1} \rangle \ll \tau$ and $\langle t_n - t_{n-1} \rangle \gg \tau$ respectively, where the averages are taken over many inter-glitch intervals.

For each glitch, we select values for s and D from probability density functions describing the distributions of glitch size and distance from Earth, $g(s)$ and $\Delta(D)$. The latter PDF is

$$\Delta(D) = Q \left(\frac{D + D_1}{D_{\odot} + D_1} \right)^a \exp \left[-b \left(\frac{D - D_{\odot}}{D_{\odot} + D_1} \right) \right], \quad (\text{A10})$$

where Q is a normalisation constant, $a = 1.64 \pm 0.11$, $b = 4.01 \pm 0.24$, $D_1 = 0.55 \pm 0.10 \text{ kpc}$, D_{\odot} is the Earth-Sun distance and D is measured from the centre of the galaxy (Faucher-Giguère & Kaspi 2006). The inter-glitch time is chosen from an exponential PDF with mean rate Θ (Melatos et al. 2008). We use Eq. (19) to evaluate $h_n(t - t_n)$.

Figure A1 graphs $h_{\times}(\tilde{t})$ for $\Theta\tau = 1$ and 10^2 (left and right respectively) and $\tilde{\omega}/(2\pi) = 1.0$. For $\Theta\tau = 1$, each glitch is distinguishable. On average, $\Theta\tau$ glitches are stacked at any given time. Glitch sizes are drawn from a power law that covers 22 decades. Feasible Monte Carlo simulations do not sample this distribution comprehensively, so that mean sampled glitch size is many orders of magnitude smaller than $\int ds s g(s)$. However, Monte-Carlo simulations used here to check the analytic theory, not to deliver actual numbers, which is deferred to a future paper. For testing purposes, a compressed s range is ample.

In the left panel of Fig. A2 we plot the mean wave strain as a function of $\Theta\tau$ for a superposition of glitches whose sizes are in the range 5×10^{-7} to 1×10^{-6} . Again, the reduced range ensures that the Monte-Carlo simulation comprehensively samples $g(s)$. A least-squares power-law fit returns a power-law index of 0.94. The mean standard deviation $\langle \sigma_h \rangle$, graphed in the right panel of Fig. A2, is also well described by a power law with index 0.64, roughly consistent with $\langle \sigma_h \rangle \propto \sqrt{\Delta N_{\nu}}$.

A3 Gravitational wave energy density

We now use the analytic expressions derived in Sec. 6 to calculate the glitch contribution to the dimensionless, cosmological, energy density parameter Ω_{gw} . We choose this quantity to make contact with other studies of stochastic gravitational-wave backgrounds, including the recent LIGO bound on theories of cosmic strings (Abbott et al. 2009). The calculation is relevant to the regime $\Theta\tau \gg 1$ (Howell et al. 2011), in which the background is continuous in time. Following Ferrari et al. (1999) and Maggiore (2000), we write Ω_{gw} as a function of wave frequency, ν , by relating it to the spectral energy density, $d^2 E_{\text{gw}}/(d\nu dS)$, through the expression

$$\Omega_{\text{gw}}(\nu) = \frac{\nu \Theta}{c^3 \rho_{\text{cr}}} \frac{d^2 E_{\text{gw}}}{d\nu dS}, \quad (\text{A11})$$

where $\rho_{\text{cr}} = 3H_0^2/(8\pi G)$ is the critical density to close the universe, H_0 is Hubble’s constant, Θ is the total event rate from Sec. A1, dS is the area element on the sky, and $E_{\text{gw}}(\nu, \mathbf{n})$ is the total energy radiated in the direction \mathbf{n} at frequency ν .

We begin the task of calculating $d^2 E_{\text{gw}}/(d\nu dS)$ by writing the energy flux from a source as (Kokkotas et al. 2001)

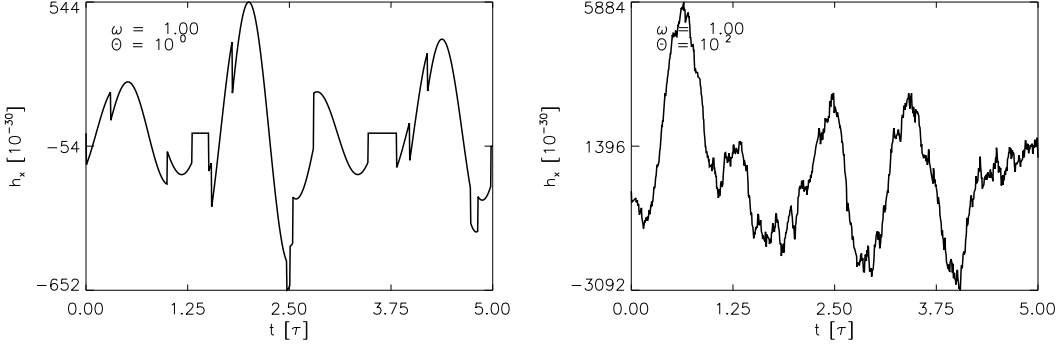


Figure A1. *Top:* Gravitational wave strain in the cross polarisation $h_{\times}(\tilde{t})$ in units of K_0/τ^2 as a function of time from glitches from multiple pulsars. The time interval is sufficient to bracket five consecutive glitches. Glitch sizes are drawn from a power-law distribution with minimum and maximum $s_{\min} = 5 \times 10^{-7}$ and $s_{\max} = 1 \times 10^{-6}$ respectively. The time between glitches is drawn from an exponential distribution with mean rate $\Theta = 1$ (*left*) and $\Theta = 10^2$ (*right*). Parameters: $\Delta\tilde{r} = 10^{-6}$, $\tau = 0.01$, $\tilde{\omega}/(2\pi) = 1$.

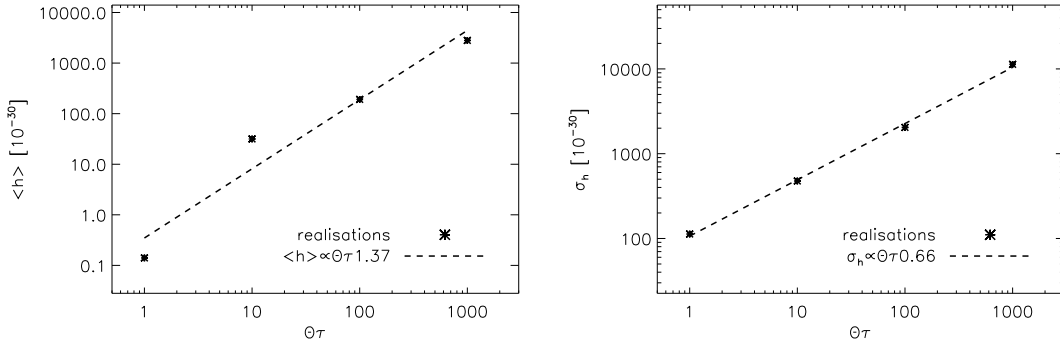


Figure A2. Mean (*left*) and standard deviation (*right*) of superposition of glitch signals for different values of Θ . Parameters: $\Delta\tilde{r} = 10^{-6}$, $\tau = 0.01$, $\tilde{\omega}/(2\pi) = 1$.

$$\frac{d^2 E}{dt dS} = \frac{c^3}{16\pi^2 G} \left| \frac{\partial h_{jk}^{TT}(t)}{\partial t} \frac{\partial h_{jk}^{TT}(t)}{\partial t} \right|. \quad (\text{A12})$$

The total radiated energy per unit area per glitch is then

$$\begin{aligned} \frac{dE_{\text{gw}}}{dS} &= \int_0^\tau dt \frac{d^2 E_{\text{gw}}}{dt dS} \\ &= \frac{c^3}{16\pi^2 G} \int_0^\infty d\nu \left| \mathcal{F} \left[\frac{\partial h_{jk}^{TT}}{\partial t} \right] \mathcal{F} \left[\frac{\partial h_{jk}^{TT}}{\partial t} \right] \right|, \quad (\text{A13}) \end{aligned}$$

where the second equality is due to Parseval's theorem and $\mathcal{F}[\cdot]$ denotes the Fourier transform. From Eq. (A13), we identify

$$\frac{d^2 E_{\text{gw}}}{d\nu dS} = \frac{c^3}{16\pi^2 G} \left| \mathcal{F} \left[\frac{\partial h_{jk}^{TT}}{\partial t} \right] \mathcal{F} \left[\frac{\partial h_{jk}^{TT}}{\partial t} \right] \right| \quad (\text{A14})$$

as the time-averaged energy flux per unit frequency. The beam pattern, $T_{jk}^{B2,21}$, which depends on the observer's position through the angles ϕ and ι (Jaranowski et al. 1998), is ensclosed in h_{jk}^{TT} . Averaging over line-of-sight orientation by integrating the right-hand side of Eq. (A14) with respect to $\cos \phi$ and ι (Jaranowski et al. 1998), we can write

$$\Omega_{\text{gw}}(\tilde{\nu}) = \frac{f_{TB2} \Theta \tilde{\nu} K_0^2}{16\pi^2 G \rho_{\text{cr}} \tau^5} \left| \mathcal{F} \left[\frac{\partial \tilde{h}_{jk}^{TT}}{\partial t} \right] \mathcal{F} \left[\frac{\partial \tilde{h}_{jk}^{TT}}{\partial t} \right] \right|, \quad (\text{A15})$$

with $\tilde{\nu} = \nu\tau$, $f_{TB2} = \int_0^{2\pi} d\phi |T^{jk, B2} T^{jk, B2}|$ and $\tilde{h}_{jk}^{TT} = (\tau^2/K_0) h_{jk}^{TT}$.

We now calculate $|\mathcal{F}[\partial \tilde{h}_{jk}^{TT}/\partial t] \mathcal{F}[\partial \tilde{h}_{jk}^{TT}/\partial t]|$ for glitches arriving from an ensemble of neutron stars. This is a stochastic quantity, because h_{jk}^{TT} depends on the random variables R_0 and ϕ_0 . The mean and variance of Ω_{gw} are found in two stages. First, we calculate $\mathcal{F}[\partial \tilde{h}_{jk}^{TT}/\partial t]$ for an individual glitch by applying the central limit theorem to add up the contributions from the ΔN_{ν} vortices involved. Second, we use properties of the χ^2 distribution to add up the signals from multiple glitches in multiple pulsars.

According to the central limit theorem, the mean and variance of $|\mathcal{F}[\partial \tilde{h}_{jk}^{TT}/\partial t] \mathcal{F}[\partial \tilde{h}_{jk}^{TT}/\partial t]|$, for a glitch involving $\Delta N_{\nu} = s N_{\nu} R_s / \Delta r$ vortices, are $\Delta N_{\nu} \mu_1$ and $\Delta N_{\nu} \sigma_1^2$ respectively [μ_1 and σ_1^2 are the Fourier transforms of Eq. (19) and Eq. (20)]. The single-vortex moments μ_1 and σ_1 are calculated by marginalising over the PDFs for initial vortex position in Eq. (17) and Eq. (18), the glitch size distribution $g(s)$, and the source distance distribution $\Delta(D)$.

The total $|\mathcal{F}[\partial \tilde{h}_{jk}^{TT}/\partial t] \mathcal{F}[\partial \tilde{h}_{jk}^{TT}/\partial t]|$ is the sum of contributions from $\Theta\tau$ simultaneous glitches. Its statistics obey

the non-central χ^2 distribution, with non-centrality parameter $\lambda_{\chi^2} = \Theta\tau\Delta N_v\mu_1^2/\sigma_1^2$, and mean and variance given by

$$\mu_\chi = \Theta\tau\sigma_1^2\Delta N_v \left(1 + \frac{\Delta N_v\mu_1^2}{\sigma_1^2}\right), \quad (\text{A16})$$

$$\sigma_\chi^2 = 2\Theta\tau\sigma_1^4\Delta N_v^2 \left(1 + \frac{2\Delta N_v\mu_1^2}{\sigma_1^2}\right). \quad (\text{A17})$$

We note that, strictly, Eq. (A16) and (A17) apply only when ΔN_v is constant. The correct expressions contain sums over different glitch sizes. However, comparison between Monte-Carlo simulations and Eq. (A16) and (A17) confirm that the approximation is reasonable. For simplicity, we also assume ω to be the same for all pulsars; the observed population of glitching pulsars is dominated by young pulsars with $10 \lesssim \omega/(2\pi) \lesssim 100$ Hz.

In the *left* panel of Fig. A3 we graph $h_\times(t)$ from Monte-Carlo simulations for $\tilde{\omega}/(2\pi) > 1$ (*top*), $\tilde{\omega}/(2\pi) = 1$ (*top centre*) and $\tilde{\omega}/(2\pi) < 1$ (*bottom centre*), representing vortex motions that are shorter, the same, and longer than one rotation period respectively. In the *right* panel, we graph the corresponding $\Omega_{\text{gw}}(\tilde{\nu})$ (*grey curves*), overplotted with analytic predictions of the mean (*asterisks*) and standard deviation (*error bars*). The error bars are too small to be seen. The *bottom* panels display results for $\tilde{\omega}/(2\pi) = 0$, where radial vortex motion is the only contributor to the gravitational wave signal.

A fair comparison between simulation and theory is achieved by restricting the glitch size to range between 5×10^{-7} and 1×10^{-6} , to ensure that the Monte-Carlo algorithm comprehensively samples $g(s)$. In all four rows in Fig. A3, the analytic mean is an excellent match to the Monte-Carlo results, but the analytic standard deviation underestimates the simulated value by a factor of ~ 100 . For $\tilde{\omega}/(2\pi) > 1$, $\Omega_{\text{gw}}(\tilde{\nu})$ peaks at $\tilde{\nu} = \tilde{\omega}/(2\pi)$ and is oscillatory, with nodes at integer multiples of $\tilde{\nu}$, except at $\tilde{\nu}_{\text{max}} = \tilde{\omega}$. For $\tilde{\omega}/(2\pi) \lesssim 1$, $\Omega_{\text{gw}}(\tilde{\nu})$ peaks at $\tilde{\nu}_{\text{max}} \approx 0.375$. The latter result holds for all $\tilde{\omega}/(2\pi) \ll 1$, because the canonical parameters listed in Table 1 describe a glitch in which vortex motion is dominated by azimuthal rather than radial motion. The peak at $\tilde{\nu}_{\text{max}} = \tilde{\omega}/(2\pi)$ is roughly five times higher than the next highest peak.

We estimate Ω_{gw} as

$$\begin{aligned} \Omega_{\text{gw}} &= \frac{K_0^2}{48\pi^2 G \rho_{\text{cr}} \tau^4} \left(\frac{2\pi\omega R_S^2}{\kappa}\right)^{3/2} \tilde{\nu}\mu_1^2 \\ &= \left(\frac{D}{10^{20} \text{ m}^{-1}}\right)^{-2} \left(\frac{\Theta}{10^2 \text{ s}^{-1}}\right)^2 \\ &\times \begin{cases} 10^{-17} \left(\frac{\tau}{10^{-2} \text{ s}}\right)^{-3} \left(\frac{\omega}{10^2 \text{ rad s}^{-1}}\right)^{5/2} \left(\frac{\Delta r}{10^{-2} \text{ m}}\right)^2, & \tilde{\omega} \gg \Delta\tilde{r} \\ 10^{-23} \left(\frac{\tau}{10^{-2} \text{ s}}\right) \left(\frac{\omega}{10^2 \text{ rad s}^{-1}}\right)^{13/2}, & \tilde{\omega} \ll \Delta\tilde{r} \end{cases} \end{aligned} \quad (\text{A18})$$

where we use $s_+ = \Delta\tilde{r}(I_s/I_c)$ and $s_- = \Delta\tilde{r}/N_v$. These results should be compared to estimates of the background from sources of cosmological origin (Maggiore 2000), such as cosmic strings [$\Omega_{\text{gw}} \sim 10^{-10}$ in the frequency range 1.5–2.5 kHz (Ferrari et al. 1999)], inflation [$\Omega_{\text{gw}} \sim 10^{-15}$ (Turner 1997)] and core-collapse supernovae [$10^{-14} \lesssim \Omega_{\text{gw}} \lesssim 10^{-12}$ at 100 Hz (Buonanno et al. 2005)].

Although the background looks relatively weak at first blush, it could be much larger than the canonical numbers in Eq. (A19) if (1) τ is smaller than 10^{-3} s, which is eminently possible, and (2) extragalactic pulsars are included, since one

has $\Theta \propto \langle D \rangle^3$ as discussed previously. These possibilities will be explored in future work.

A4 Signal to noise

The optimised signal-to-noise ratio (S/N) for an integration time T is given by (Allen & Romano 1999)

$$\frac{S}{N} = \left[\frac{9H_0^4 T}{50\pi^4} \int_0^\infty d\nu \frac{\gamma^2(\nu)\Omega_{\text{gw}}^2(\nu)}{\nu^6 P_1(\nu)P_2(\nu)} \right]^{1/2}, \quad (\text{A20})$$

where $P_1(\nu)$ and $P_2(\nu)$ are the power spectral noise densities for the two detectors, and γ is the normalised overlap reduction function, which characterises the loss of sensitivity due to the separation and relative orientation of the detectors. The minimum observable Ω_{gw} of two detectors with the sensitivity of the Einstein Telescope (with a signal-to-noise ratio of 2.56) is $\Omega_{\text{min}} = 1.13 \times 10^{-11}$ for an integration time of one year, a false alarm rate of $\alpha = 10\%$, and a detection rate of 90% (Marassi et al. 2010). For $\omega/(2\pi) = 200$ Hz, and assuming a Milky Way distance distribution given by Eq. (A10), with an aggregate glitch rate of $\Theta = 10^2 \text{ s}^{-1}$, and glitches lasting $\tau = 0.01$ s, we obtain $S/N = 10^{-4}$ for Milky Way glitches (with $\gamma = 1$ for simplicity). Very crudely, assuming there are $\sim 10^{10}$ Milky-Way type galaxies, evenly distributed throughout the universe, $S/N \propto \Omega_{\text{gw}} \propto \langle D \rangle$ becomes ~ 1 .

REFERENCES

- Abadie J., Abbott B. P., Abbott R., Adhikari R., Ajith P., Allen B., Allen G., Amador Ceron E., Amin R. S., Anderson S. B., et al. 2011, PRD, 83, 042001
 Abbott B. P., Abbott R., Acernese F., Adhikari R., Ajith P., Allen B., Allen G., Alshourbagy M., Amin R. S., Anderson S. B., et al. 2009, Nature, 460, 990
 Abrikosov A. A., 1957, Sov. Phys. - JETP (Engl. Transl.), 5, 1174
 Allen B., Romano J. D., 1999, PRD, 59, 102001
 Alpar M. A., Anderson P. W., Pines D., Shaham J., 1981, PNAS, 78, 5299
 Alpar M. A., Cheng K. S., Pines D., 1989, ApJ, 346, 823
 Alpar M. A., Pines D., Anderson P. W., Shaham J., 1984, ApJ, 276, 325
 Alpar M. A., Sauls J. A., 1988, ApJ, 327, 723
 Anderson P. W., Alpar M. A., Pines D., Shaham J., 1982, Phil. Mag. A, 45, 227
 Anderson P. W., Itoh N., 1975, Nature, 256, 25
 Andersson N., Comer G., Prix R., 2004, MNRAS, 354, 101
 Andersson N., Comer G. L., 2001, PRL, 87, 241101
 Andersson N., Comer G. L., Prix R., 2004, MNRAS, 354, 101
 Avogadro P., Barranco F., Broglia R., Vigezzi E., 2008, Nuclear Physics A, 811, 378
 Bennett M. F., van Eysden C. A., Melatos A., 2010, MNRAS, pp 1370–+
 Buonanno A., Sigl G., Raffelt G. G., Janka H.-T., Müller E., 2005, PRD, 72, 084001
 Cheng K., Pines D., Alpar M., Shaham J., 1988, ApJ, 330, 835
 Chukwude A. E., Urama J. O., 2010, MNRAS, 406, 1907

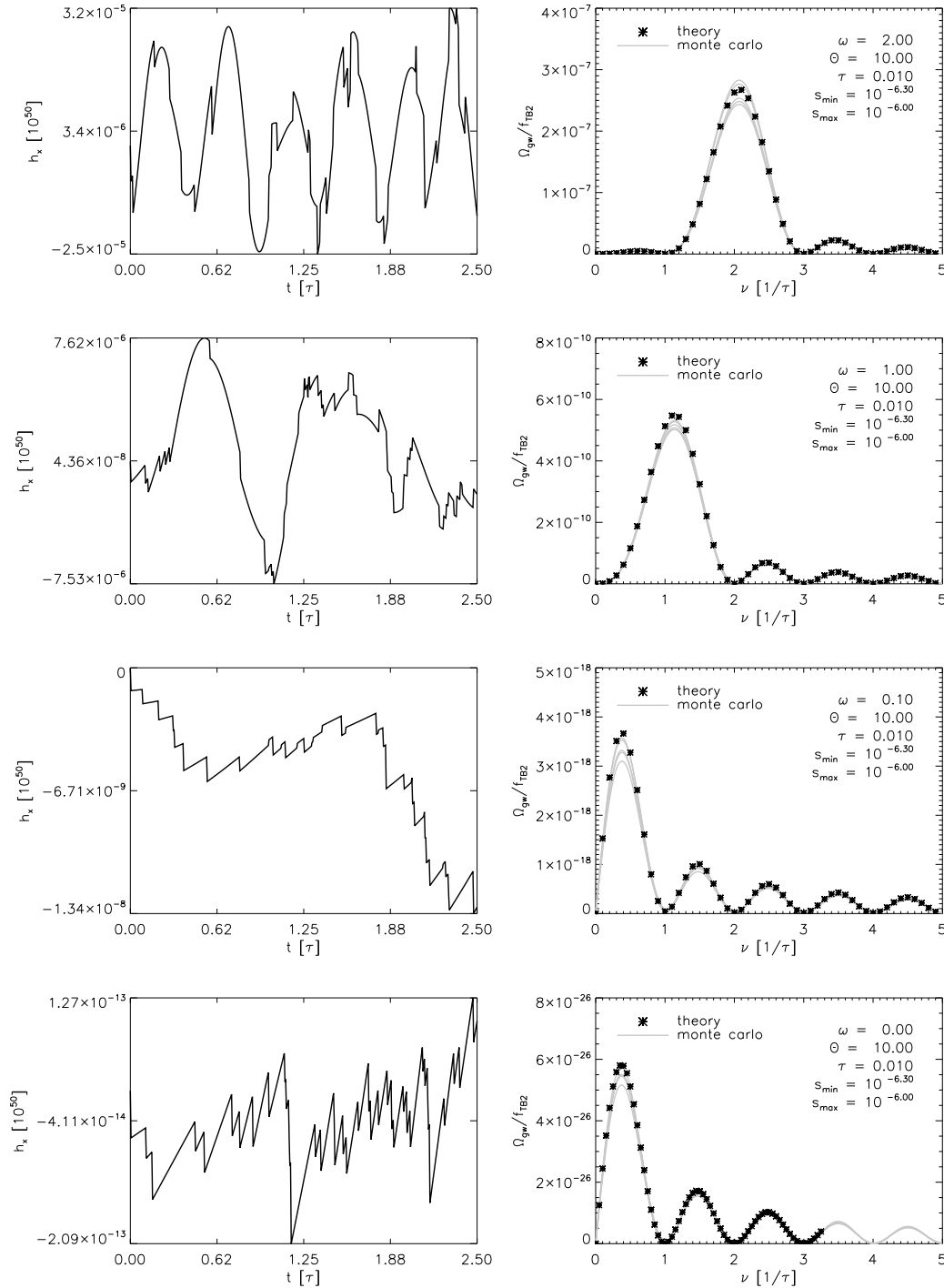


Figure A3. Superposition of gravitational wave signals in the cross polarisation $h_{\times}(t)$ (in units of K_0/τ^2 ; *left column*) and gravitational wave energy density parameter, $\Omega_{\text{gw}}(\nu)$ (*right column*), from a population of glitching pulsars with mean aggregate glitch rate $\Theta = 10$, for $\tilde{\omega}/(2\pi) = 2.0, 1.0, 0.1$ and 0 (*top to bottom* respectively). The *grey* curves in the *right* column are different realisations of the underlying glitch size and distance distributions. The *asterisks* correspond to the theoretical calculation described in Sec. A. Minimum and maximum glitch sizes are 5×10^{-7} and 10^{-6} respectively. Unless otherwise stated, the pulsar parameters are given in Table. 1.

- Clark J., Heng I. S., Pitkin M., Woan G., 2007, PRD, 76, 043003
- Crawford F., Demiański M., 2003, ApJ, 595, 1052
- Daly E., Porporato A., 2007, PRE, 75, 11119
- Epstein B., Van Riper K., 1992, Nature, 359, 616
- Espinoza C. M., Lyne A. G., Stappers B. W., Kramer M., 2011, astro-ph.HE/1102.1743
- Faucher-Giguère C., Kaspi V. M., 2006, ApJ, 643, 332
- Ferrari V., Matarrese S., Schneider R., 1999, MNRAS, 303, 258
- Flanagan C. S., Buchner S. J., 2006, Central Bureau Electronic Telegrams, 595, 1
- Glampedakis K., Andersson N., 2009, PRL, 102, 141101
- Goldbaum D. S., Mueller E. J., 2009, PRA, 79, 63625
- Harris T. E., 1989, The Theory of Branching Processes. Dover, New York
- Haskell B., Pizzochero P., Sidery T., 2011, ArXiv e-prints 1107.5295
- Hayama K., Desai S., Mohanty S. D., Rakhmanov M., Summerscales T., Yoshida S., 2008, CQG, 25, 184016
- Howell E., Regimbau T., Corsi A., Coward D., Burman R., 2011, MNRAS, 410, 2123
- Jackson B., Barengi C. F., 2006, PRA, 74, 043618
- Jahan-Miri M., 2005, JLTP, 139, 373
- Janssen G. H., Stappers B. W., 2006, A&A, 457, 611
- Jaranowski P., Królak A., Schutz B. F., 1998, PRD, 58, 063001
- Jones P. B., 1991, ApJ, 373, 208
- Kokkotas K. D., Apostolatos T. A., Andersson N., 2001, MNRAS, 320, 307
- Link B., Epstein R. I., 1996, ApJ, 457, 844
- Lyne A. G., Shemar S. L., Smith F. G., 2000, MNRAS, 315, 534
- McKenna J., Lyne A., 1990, Nature
- Maggiore M., 2000, Physics Reports, 331, 283
- Manchester R. N., Hobbs G. B., Teoh A., Hobbs M., 2005, The Astron. J., 129, 1993
- Marassi S., Ciolfi R., Schneider R., Stella L., Ferrari V., 2010, astro-ph.CO/1009.1240
- Melatos A., Peralta C., 2010, ApJ, 709, 77
- Melatos A., Peralta C., Wyithe J. S. B., 2008, ApJ, 672, 1103
- Melatos A., Warszawski L., 2009, ApJ, 700, 1524
- Middleditch J., Marshall F. E., Wang Q. D., Gotthelf E. V., Zhang W., 2006, ApJ, 652, 1531
- Mink M. P., Smith C. M., Duine R. A., 2009, PRA, 79, 013605
- Negi P. S., 2010, Astrophysics & Space Science, pp 296–+
- Peralta C., Melatos A., 2009, ApJL, 701, L75
- Peralta C., Melatos A., Giacobello M., Ooi A., 2006a, ApJ, 635, L53
- Peralta C., Melatos A., Giacobello M., Ooi A., 2006b, ApJ, 651, 1079
- Pines D., Shaham J., Alpar M. A., Anderson P. W., 1980, Prog. Theor. Phys., 69, 376
- Prix R., Giampanis S., Messenger C., 2011
- Regimbau T., de Freitas Pacheco J. A., 2006a, A&A, 447, 1
- Regimbau T., de Freitas Pacheco J. A., 2006b, ApJ, 642, 455
- Ruderman M., 1969, Nature, 223, 597
- Sato T., Ishiyama T., Nikuni T., 2007, PRA, 76, 53628
- Sidery T., Passamonti A., Andersson N., 2010, MNRAS, 405, 1061
- Thorne K. S., 1980, Reviews of Modern Physics, 52, 299
- Thrane E., et al., 2010, astro-ph/1012.2150
- Turner M. S., 1997, PRD, 55, R435
- van Eysden C., Melatos A., 2008, CQG, 25
- Warszawski L., Melatos A., 2008, MNRAS, 390, 175
- Warszawski L., Melatos A., 2011, MNRAS, 415, 1611
- Warszawski L., Melatos A., Berloff N. G., 2012, PRB, 85, 104503
- Wasserman I., 2008, Gravitational Radiation from nonaxisymmetric vorticity fluctuations in neutron stars, Priv. Comm.